

# Androgens drive SLC1A5-dependent metabolic reprogramming in polycystic ovary syndrome

Received: 10 November 2024

Accepted: 4 August 2025

Published online: 15 August 2025

 Check for updates

Yishu Wang <sup>1,2,6</sup>, Jiaying Wu<sup>1,2,6</sup>, Gaochen Zhang<sup>2</sup>, Yan Shi<sup>2</sup>, Yicong Meng<sup>1,2</sup>, Pingping Lv<sup>3</sup>, Weiwei Huang<sup>2</sup>, Yunfei Su<sup>2</sup>, Zhiyang Zhou<sup>2</sup>, Bo Wang<sup>4</sup>, Xiaojun Chen<sup>1</sup>, Chengliang Zhou<sup>1</sup>, Jiexue Pan <sup>2,5</sup>, Li Jin<sup>2,5</sup>, Xiaotao Wang <sup>2</sup>, Yanting Wu <sup>2,5</sup>, Jianzhong Sheng <sup>2,3</sup>, Xinmei Liu <sup>2</sup>, Yu Zhang <sup>2</sup> ✉, Guolian Ding <sup>2,5</sup> ✉, Chuanjin Yu <sup>2</sup> ✉ & Hefeng Huang <sup>1,2,3,5</sup> ✉

Polycystic ovary syndrome is the primary cause of female infertility. Growing evidence suggests that dysregulation of amino acid metabolism plays a significant role in the onset and progression. However, the underlying mechanism remains unclear. In this study, we conduct targeted metabolite profiling of human follicular fluid and granulosa cells. A significant increase in glutamine uptake is observed in patients with hyperandrogenic polycystic ovary syndrome, mediated by the upregulation of SLC1A5, a specific glutamine transporter. We find that androgen excess primarily activates SLC1A5 expression. Furthermore, SLC1A5 overexpression in female mice induces polycystic ovary syndrome-like phenotypes, including hyperandrogenism and abnormal follicle development. Additionally, the pharmacological blockade of SLC1A5 provides reproductive benefits to mice exhibiting polycystic ovary syndrome-like symptoms. Mechanistically, we show that elevated flux of Gln-derived  $\alpha$ -ketoglutarate enhances HDAC5 expression and suppresses acetylation on histone 3 lysine residue 14 and lysine residue 56. The reduction in acetylation level is associated with the downregulation of several genes related to folliculogenesis, including *CYP19A1*, thereby exacerbating androgenic homeostasis imbalance. These findings indicate that androgen-induced aberrant glutamine uptake via SLC1A5 is crucial for the development and progression of polycystic ovary syndrome, suggesting pharmacological blockade of SLC1A5 as a potential therapeutic strategy.

Polycystic ovary syndrome (PCOS) has a prevalence ranging from 10% to 20% and is among the most common endocrine and metabolic disorders affecting premenopausal women<sup>1–4</sup>. Heterogeneous by nature, PCOS is the primary cause of anovulatory infertility. It is characterized by various endocrine abnormalities, including hyperandrogenism, oligo-ovulation or anovulation, and polycystic ovarian morphology<sup>5–7</sup>.

Additionally, PCOS often encompasses a variety of metabolic disorders, such as insulin resistance, obesity, type 2 diabetes (T2D), hypertension, and cardiovascular diseases<sup>8</sup>. The insufficient understanding of the etiology and pathophysiology of PCOS results in current therapies being suboptimal, only providing partial symptom relief. There is an urgent need for preventive and targeted treatments.

A full list of affiliations appears at the end of the paper. ✉ e-mail: [zhang\\_yu\\_sfy@fudan.edu.cn](mailto:zhang_yu_sfy@fudan.edu.cn); [dingguolian@fudan.edu.cn](mailto:dingguolian@fudan.edu.cn); [yuchuanjin1013@163.com](mailto:yuchuanjin1013@163.com); [huanghefg@hotmail.com](mailto:huanghefg@hotmail.com)

Granulosa cells (GCs) and oocytes function as an integral morphological and functional unit, exhibiting a close association and interdependent<sup>9,10</sup>. The oocyte partly relies on nutrients and growth regulators secreted by GCs, while also participating in the proliferation, development, and function of the follicular GCs<sup>11</sup>. Consequently, abnormal metabolism of GCs is likely to result in disorders of ovarian development. Considerable attention has been directed towards the roles of glucose and lipid metabolism in influencing follicle developmental competence. Our previous research has shown that phosphoglycerate kinase (PGK1) induces glucose metabolic disorders in GCs, thereby exacerbating androgen-induced cytotoxicity<sup>12</sup>. Additional studies have confirmed the presence of active lipid metabolism in GCs from women with PCOS, primarily involving the energy synthesis and the steroid hormone production pathways<sup>13</sup>. Recent evidence highlights the significance of amino acid dysregulation in GCs in the occurrence and progression of PCOS. Elevated plasma levels of branched-chain amino acids (BCAAs) in women with PCOS are significantly associated with insulin resistance and metabolic syndrome<sup>14</sup>. Defects in the BCAA metabolism-related gene, protein phosphatase Mg<sup>2+</sup>/Mn<sup>2+</sup>-dependent 1 K (PPMIK), can disrupt energy metabolism homeostasis within the follicular microenvironment, potentially leading to PCOS-like phenotypes<sup>15</sup>. Furthermore, follicle-stimulating hormone (FSH) regulates glutamine (Gln) levels in follicular fluid (FF) and influences ovulation via ASK1-JNK-mediated GC apoptosis. This mechanism elucidates the challenges faced by patients with PCOS during the selection of the dominant follicle and pre-ovulatory maturation stages of folliculogenesis<sup>16</sup>.

Gln is a conditionally essential amino acid whose biosynthesis is often insufficient to adequately respond to cell demands, particularly under certain physio-pathological conditions. Gln-mediated anaplerosis begins with the uptake of Gln via the solute carrier (SLC) family of transporters, predominantly SLC1A5<sup>17</sup>. Once inside the cell, Gln can undergo various metabolic pathways. After being converted to glutamate (Glu) by the enzyme glutaminase (GLS), Gln is further transformed to  $\alpha$ -ketoglutarate ( $\alpha$ -KG), entering the mitochondrial tricarboxylic acid (TCA) cycle for energy production. Additionally, Gln functions as a biosynthetic precursor and a scavenger of reactive oxygen species (ROS), playing a role in regulating amino acid pools. Previous studies have reported that androgen significantly enhances the expression of Gln transporters and promotes Gln uptake in androgen receptor (AR)-sensitive prostate cancer cells<sup>18,19</sup>, indicating a close relationship between androgen and glutaminolysis. Hyperandrogenism is a fundamental component of the pathophysiology of PCOS and primarily drives various phenotypic features, including follicular dysplasia, impaired ovulation, endometrial disorders, and metabolic dysfunction<sup>20–22</sup>. However, it remains unclear whether the abnormal Gln metabolism in GCs is causally linked to the risk of hyperandrogenism in PCOS or if the relationship is reversed.

In this study, we screened metabolites in both FF and GCs, finding that elevated Gln uptake in GCs was significantly associated with hyperandrogenism in women with PCOS. We performed transcriptome analysis to characterize critical metabolic genes in GCs and identified *SLC1A5*, a specific Gln transporter, as the key molecule associated with PCOS-related hyperandrogenism. Furthermore, we developed a mouse model with *SLC1A5*-overexpression and treated PCOS-like mice with an *SLC1A5* inhibitor to investigate if aberrant Gln metabolism could induce PCOS-like characteristics. Finally, we analyzed the metabolic flux of Gln in human ovarian GCs and found that Gln-derived  $\alpha$ -KG altered histone acetylation levels of several genes related to folliculogenesis, contributing to the risk of infertility caused by ovulation disorders in PCOS patients.

## Results

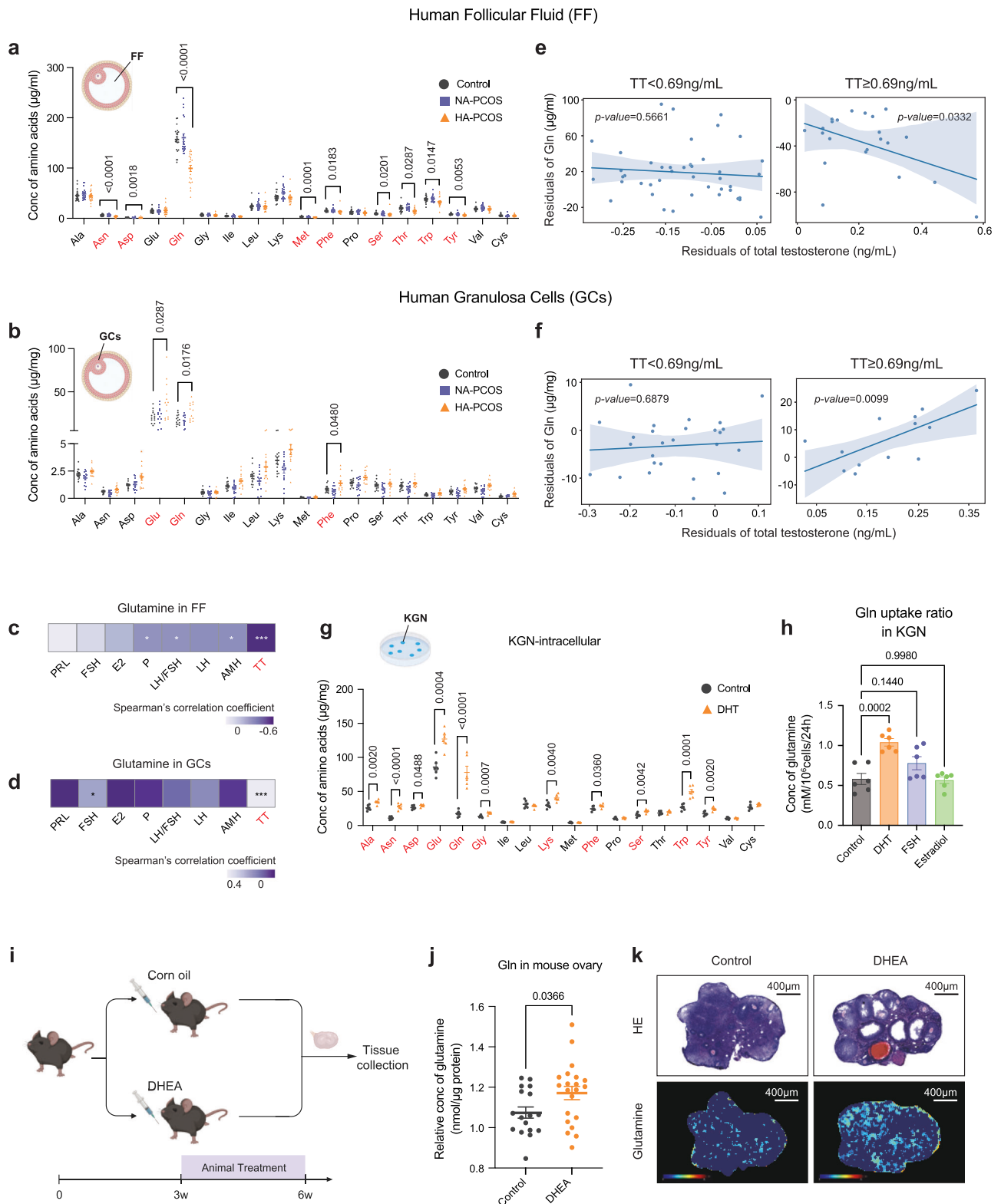
### Hyperandrogenic-PCOS patients exhibit elevated glutamine uptake in GCs

To explore the association between amino acid metabolites and PCOS clinical characteristics, a targeted metabolomic survey was conducted

on the amino acid metabolites in both FF and GCs of 43 patients with PCOS and 22 age-matched individuals as controls. The basic characteristics of PCOS patients and controls are listed in Supplementary Data 1. Among the PCOS group, those with serum total testosterone (TT) levels greater than or equal to 0.69 ng/mL, which was calculated based on the standard curve (Supplementary Fig. 1a), were defined as hyperandrogenic-PCOS (HA-PCOS), while the rest were normoandrogenic PCOS (NA-PCOS), as a previous study reported<sup>23</sup>. The levels of asparagine (Asn), aspartate (Asp), Gln, methionine (Met), phenylalanine (Phe), serine (Ser), threonine (Thr), tryptophan (Trp), and tyrosine (Tyr) in FF were significantly lower in the HA-PCOS group than in the control group (Fig. 1a). In contrast, the intracellular Glu, Gln and Phe levels in GCs were higher in HA-PCOS patients, but not in the NA-PCOS GCs (Fig. 1b). Considering that Gln exhibits significantly higher abundance in FF and GCs with divergent concentration trends, it captured our particular interest. When analyzing all enrolled patients (including both control and PCOS groups), Gln levels in FF showed a negative correlation with TT, anti-Müllerian hormone (AMH), progesterone (P), and the luteinizing hormone (LH) to FSH ratio, with TT exhibiting the most significant relationship (Fig. 1c). Among the indicators mentioned above, only TT levels demonstrated a significant positive correlation with Gln levels in GCs (Fig. 1d). In the subgroup analysis adjusted for potential confounding factors (age and BMI), patients were stratified based on TT concentration (0.69 ng/mL). It is interesting that only in the HA-PCOS group (when the TT level exceeds 0.69 ng/mL), the negative correlation between TT and Gln levels in FF and the positive correlation between TT and Gln levels in GC were most significant (Fig. 1e, f). When TT < 0.69 ng/mL, no significant correlation was observed between Gln and TT levels in FF and GC samples, regardless of the control group or NA-PCOS (Fig. 1e, f). These results indicated that in HA-PCOS patients, the Gln content in FF is significantly reduced, while the Gln level in GC is significantly increased, which is closely related to androgen levels.

We further conducted *in vitro* experiments. The human ovarian granulosa-like tumor cell line (KGN) was treated with dihydrotestosterone (DHT), the biologically active metabolite of TT, and found a significant increase in the levels of Gln, as well as metabolites such as Glu and Phe (Fig. 1g), consistent with those observed in clinical GCs from the HA-PCOS patients. Moreover, DHT treatment increased the uptake of Gln by KGN cells, whereas FSH and estradiol (E2) treatment had no significant effect on Gln uptake (Fig. 1h). For *in vivo* study, we established dehydroepiandrosterone (DHEA)-induced PCOS-like mouse model (Fig. 1i), and found that compared with the control group, the levels of Gln significantly increased in the ovaries of DHEA group (Fig. 1j). Moreover, spatially specific detection of glutamine content in mouse ovaries revealed an obvious increase in Gln levels within granulosa cells of the DHEA group (Fig. 1k). Therefore, both *in vitro* and *in vivo* experiments validated that hyperandrogen could induce intracellular Gln elevation in GCs.

To investigate the potential mechanism of elevated Gln uptake in GC cells, we detected and analyzed the RNA-seq data of ovarian GCs from control, NA-PCOS, and HA-PCOS women. Among the differentially expressed genes between the control group and HA-PCOS group, *SLC1A5*, one of the best-characterized Gln transporters so far<sup>19</sup>, was significantly increased (Fig. 2a). The gene set enrichment analysis (GSEA) results revealed that, compared to the control group, upregulated pathways in HA-PCOS were significantly enriched in pathways such as protein transmembrane transporter activity, protein N-linked glycosylation, oxidative phosphorylation, and glycolysis (Fig. 2b). The increased expression of *SLC1A5* in GCs of HA-PCOS patients was also validated at the mRNA and protein levels (Fig. 2c–e). Furthermore, we assessed the expression profiles of other common Gln transporters and metabolic enzymes and observed no statistically significant alterations in their expression levels (Supplementary Fig. 1b, c). To explore the function of *SLC1A5* in GCs, we then overexpressed *SLC1A5*



(designated as OE-SLC1A5) in KGN cells, and found the Gln uptake ratio was increased in OE-SLC1A5 KGN cells (Fig. 2f). The targeted metabolomic survey also showed an increase in intracellular Gln levels in OE-SLC1A5 KGN cells (Fig. 2g), indicating that SLC1A5 is the key regulatory factor in androgen-driven upregulation of Gln uptake. In addition, DHT treatment upregulated the mRNA and protein levels of SLC1A5 in KGN in a dose-dependent manner (Fig. 2h, i).

The protein band of SLC1A5 shifted after the treatment of peptide-N-glycosidase F (PNGase F), which can specifically catalyze the removal

of N-linked sugar chains and accurately break covalent bonds between sugar chains and proteins, implying the high fundamental N-glycosylated level of SLC1A5 in KGN cells (Supplementary Fig. 1d). The N-linked glycosylation status of SLC1A5 has been investigated as necessary for the definitive localization in the plasma membrane, without which the amino acid transporter function was damaged<sup>16</sup>. DHT increased several N-linked glycosylation enzyme expressions (Supplementary Fig. 1e) and upregulated N-linked glycosylation levels of SLC1A5 in KGN cells and murine ovarian GCs (Supplementary

**Fig. 1 | The Gln uptake increases in GCs of HA-PCOS patients and the ovaries of PCOS-like mice.** **a, b** Targeted metabolomic profile on FF (**a**) and GCs (**b**) of clinical patients. The FF samples were collected from Control ( $n = 22$ ), NA-PCOS ( $n = 21$ ), and HA-PCOS ( $n = 22$ ), and the GC samples were collected from Control ( $n = 14$ ), NA-PCOS ( $n = 13$ ), and HA-PCOS ( $n = 13$ ). **c, d** Correlation of Gln levels in FF (**c**) and GCs (**d**) with the levels of hormones, as determined by Spearman's rank test.  $*p < 0.05$ ,  $***p < 0.001$ . **e, f** The correlation of the residuals of Gln levels in FF (**e**) and GCs (**f**) with the residuals of TT levels, adjusted for age and BMI. **g** Targeted metabolomic profile on DHT-treated KGN cells ( $10^{-7}$  mol/L, 24 h,  $n = 6$ ). **h** Gln uptake ratio of KGN cells treated with DHT, FSH, and Estradiol ( $10^{-7}$  mol/L, 24 h,  $n = 6$  for each group). **i** Workflow of DHEA-induced PCOS-like model. Created in BioRender. Ye, L. (2025)

<https://BioRender.com/yb2yu8f>. **j** Gln levels in murine ovaries (Control  $n = 17$ , DHEA  $n = 21$ ). **k** Representative images of hematoxylin and eosin (HE) staining and MALDI mass spectrometry imaging of Gln on murine ovaries (scale bar: 400  $\mu$ m). The experiment was repeated three times independently with similar results. For statistical analysis, one-way ANOVA followed by Tukey's multiple comparisons tests, Welch's ANOVA followed by Dunnett's T3 multiple comparisons tests, and Kruskal-Wallis tests followed by Dunn's multiple comparisons tests were performed in (**a, b, h**); linear regression analyses were performed in (**e, f**); Student's t tests and Mann-Whitney tests were performed in (**g, j**). Data are presented as the mean  $\pm$  SEM. All tests were two-sided. Source data are provided as a Source Data file.

Fig. 1f, g). These findings indicated that androgen may increase Gln uptake through elevated SLC1A5 expression as well as N-glycosylation levels of SLC1A5.

Given the positive correlation between TT levels, SLC1A5 expression, and the Gln uptake ratio, we hypothesized that androgens may directly regulate SLC1A5 expression and subsequent Gln uptake. To test this hypothesis and investigate the role of AR under more physiological conditions, we assessed the effect of AR on DHT-induced SLC1A5 expression. The Stacc-seq analysis revealed that DHT strongly promoted AR recruitment to the SLC1A5 promoter (Fig. 2j). Taken together, these data indicated that androgen increases SLC1A5 expression and the following Gln uptake through AR signaling.

### SLC1A5 overexpression induces PCOS-like traits and subdues fertility

We previously confirmed a strong association between SLC1A5 expression and HA-PCOS, and we next aimed to investigate whether SLC1A5 overexpression can directly trigger the development of PCOS. To better understand the phenotypic association of SLC1A5 with PCOS, adeno-associated virus (AAV) was injected into the bilateral ovaries in situ to construct a *Slc1a5*-overexpressing mouse model, designated as AAV-Slc1a5 mice (Fig. 3a). AAV-Slc1a5 mice exhibited PCOS-like traits, characterized by fewer proestrus and estrous cycles and an increase in metestrus and diestrus cycles compared to control mice (Fig. 3b). Notably, an increased number of primary and secondary follicles, alongside fewer antral follicles, was observed in AAV-Slc1a5 mice (Fig. 3c, d). This supports the hypothesis that the excessive proliferation of small follicles contributes to PCOS-related infertility, as evidenced by reduced GC apoptosis and thicker, more rapidly proliferating GC layers in the follicles of AAV-Slc1a5 mice (Supplementary Fig. 2a). Additionally, AAV-Slc1a5 mice recapitulated the neuroendocrine traits of PCOS, including elevated serum levels of TT, AMH, and LH/FSH ratio (Fig. 3e–g).

To further investigate the impact of SLC1A5 on fertility, AAV-Slc1a5 mice and littermate control females were each mated with wild-type males. AAV-Slc1a5 mice displayed a lower fertility index and produced fewer pups per litter, while there was no significant difference in the time to first litter (Fig. 3h, Supplementary Fig. 2b, c). MII oocytes were collected from 7-week-old mice superovulated with 5 IU of PMSG and hCG, revealing dynamic changes in folliculogenesis and a suboptimal ovarian response in AAV-Slc1a5 mice compared to controls (Fig. 3i, Supplementary Fig. 2d). Furthermore, overexpression of SLC1A5 resulted in meiotic failure in mouse oocytes, as indicated by a lower frequency of first polar body extrusion (Supplementary Fig. 2e) and a reduced ratio of 2-cell embryos (Supplementary Fig. 2f, g). In summary, the overexpression of SLC1A5 directly leads to PCOS-like phenotype and fertility impairment in mice.

### Inhibition of SLC1A5 confers reproductive and metabolic benefits to PCOS-like mice

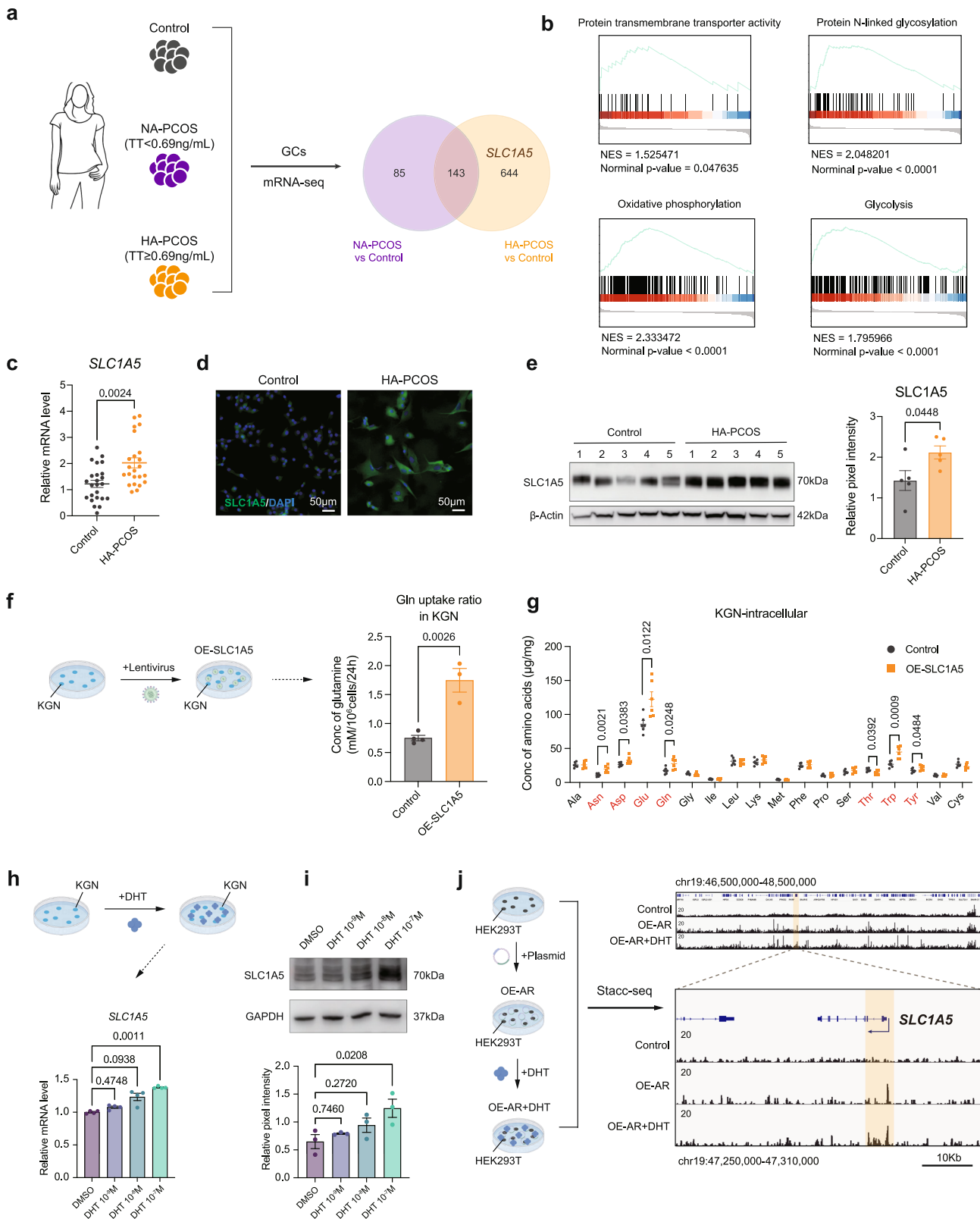
To further confirm that SLC1A5 influences neuroendocrine disturbances in PCOS, we treated a DHEA-induced PCOS-like mouse model (designated as DHEA mice) with the SLC1A5 inhibitor, GPNA (designated as

DHEA + GPNA mice) (Fig. 4a). Following a one-month intraperitoneal injection of GPNA, the elevated expression of SLC1A5 in the ovaries and GCs of DHEA mice was reduced to levels comparable to those of control mice (Fig. 4b–e). Furthermore, GPNA alleviated the presence of multiple cyst-like follicles with collapsed walls in DHEA mice (Fig. 4b). GPNA treatment decreased serum TT, AMH, and the LH/FSH ratio (Fig. 4f–h) and restored the regular estrous cycle in DHEA mice (Fig. 4i, j). Additionally, GPNA improved glucose tolerance in DHEA mice (Supplementary Fig. 3a) and increased insulin sensitivity (Supplementary Fig. 3b, c), as demonstrated by glucose tolerance tests (GTT) and insulin tolerance tests (ITT). DHEA + GPNA mice exhibited lower body weight (Supplementary Fig. 3d) and subcutaneous fat mass compared to the DHEA group (Supplementary Fig. 3e–g). Moreover, GPNA treatment significantly reduced plasma levels of high-density lipoprotein cholesterol (HDL-C), which were elevated in DHEA mice (Supplementary Fig. 3h). These results suggested that SLC1A5 inhibition through GPNA effectively mitigates neuroendocrine disturbances and metabolic dysfunctions associated with PCOS in the DHEA-induced mouse model.

### SLC1A5 mediates energy metabolism and redox regulation

SLC1A5 primarily functions in Gln uptake. Therefore, we investigated how upregulation of SLC1A5 and the subsequent increase in Gln uptake and accumulation in GCs contribute to the development of PCOS. Gln fuels the TCA cycle, macromolecular biosynthesis, and redox homeostasis<sup>24–27</sup>. Since rapidly proliferating cells frequently develop Gln addiction, we assessed the impact of SLC1A5 on KGN cell growth. Overexpression of SLC1A5 significantly promoted cell growth, which could be inhibited by GPNA (Fig. 5a). SLC1A5 controls ROS scavenging by generating GSH. Redox regulation is essential for follicle development, and therefore, we investigated the impact of SLC1A5 on the redox homeostasis of KGN cells. Gln regulates ROS by serving as a crucial source for glutathione (GSH) synthesis. SLC1A5 overexpression increased the cellular GSH/GSSG ratio (Fig. 5b) and suppressed cellular and mitochondrial ROS levels (Fig. 5c, d). In contrast, inhibition of SLC1A5-derived GSH synthesis by GPNA (Fig. 5b) significantly increased cellular and mitochondrial ROS levels (Fig. 5c, d). Mitochondrial oxidative stress causes mitochondrial damage. We further examined mitochondrial dynamics and observed damaged mitochondrial morphology (Fig. 5e) and a decreased mitochondrial membrane potential (MMP) following SLC1A5 knockdown (Fig. 5f). Additionally, knockdown of SLC1A5 suppressed the GSH/GSSG ratio and increased cellular and mitochondrial ROS levels (Fig. 5g–i), indicating that SLC1A5 is responsible for Gln regulation of cellular ROS homeostasis.

To further investigate the role of SLC1A5 in energy use, we measured the extracellular acidification rate (ECAR) and the oxygen consumption rate (OCR) in KGN cells with a real-time metabolite analyzer. The basal and maximal ECAR and OCR levels were higher in OE-SLC1A5 KGN cells (Fig. 5j, k), suggesting a more aerobic and energetic cell type. GPNA treatment suppressed the increased basal and maximal ECAR and OCR associated with SLC1A5 overexpression (Fig. 5j, k). Conversely, SLC1A5 knockdown impaired both basal and maximal ECAR and OCR (Fig. 5l, m), resulting in a more quiescent and glycolytic cell type. These data support that SLC1A5 contributes to mitochondrial



oxidative phosphorylation and glycolysis via enhanced Gln influx, driving the metabolic reprogramming in KGN cells.

**Gln-derived α-KG accumulation in GCs impairs follicle development**

The TCA cycle is crucial for cellular oxidative phosphorylation and fulfills the bioenergetic, biosynthetic, and redox balance

requirements<sup>28</sup>. Thus, we explored whether SLC1A5 could enhance TCA cycle metabolites in GCs through mitochondrial glutaminolysis (Fig. 6a). Upregulation of SLC1A5 increased the concentration of several Gln-derived TCA cycle metabolites, including Glu, α-KG, citrate, malate, and fumarate (Fig. 6b-f), while no changes were observed in succinate, a downstream product of α-KG (Fig. 6g). Conversely, downregulation of SLC1A5 (Supplementary Fig. 4a)

**Fig. 2 | The SLC1A5-dependent Gln uptake is induced by androgen.** **a** The overlapping DEGs of GCs by RNA-seq analysis ( $n = 6$  for each group). **b** GSEA analysis in GCs of HA-PCOS compared with Control. **c** qPCR was performed to assess the expression levels of *SLC1A5* in Control ( $n = 24$ ) and HA-PCOS ( $n = 23$ ). **d** IF staining was performed to visualize the expression of *SLC1A5* in human GCs (scale bar: 50  $\mu\text{m}$ ). The experiment was repeated three times independently with similar results. **e** WB and densitometric analysis of *SLC1A5* expression in human GCs from Control and HA-PCOS ( $n = 5$  for each group).  $\beta$ -Actin was denoted as an internal reference protein. **f** Gln uptake ratio of OE-*SLC1A5* KGN cells (Control  $n = 4$ , OE-*SLC1A5*  $n = 3$ ). **g** Targeted metabolomic profile on *SLC1A5*-overexpressed KGN cells ( $n = 6$ ). **h**, **i** qPCR (**h**) and WB analysis (**i**) of *SLC1A5* expression in KGN cells treated with different doses of DHT for 2 h ( $n = 3$  for each group). **j** Stacc-seq analysis was

performed to identify binding peaks of AR in HEK293T cells. The Stacc-seq data were visualized using IGV. Peaks were identified as regions of significant enrichment on the promoter region of *SLC1A5* (indicated by yellow) and correspond to the binding sites of AR. The plasmids were transfected into HEK293T for 24 h, followed by DHT treatment ( $10^7$  mol/L) for another 24 h ( $n = 2$ ). For statistical analysis, GSEA of selected GO-BP terms was performed using the R package clusterProfiler (v4.16.0) in (**b**); Mann-Whitney test was performed in (**c**); Student's *t* tests were performed in (**e-g**); Kruskal-Wallis tests with Dunn's tests were performed in (**h**); one-way ANOVA followed by Dunnett's tests were performed in (**i**). Data are presented as the mean  $\pm$  SEM. All tests were two-sided. Source data are provided as a Source Data file.

concomitantly decreased the concentration of Glu and  $\alpha$ -KG (Supplementary Fig. 4b, c), while other TCA intermediate metabolites remained unaffected (Supplementary Fig. 4d-g). Collectively, these results indicated that *SLC1A5*-derived Gln uptake resulted in  $\alpha$ -KG accumulation in GCs. The findings were further validated in OE-*SLC1A5* and sh-*SLC1A5* KGN cells (Fig. 6h). What's more,  $\alpha$ -KG accumulation was also found in the ovaries of AAV-*Slc1a5* mice (Fig. 6i) and DHEA-induced PCOS-like mice (Supplementary Fig. 4h).

The incorporation of  $\alpha$ -KG into the TCA cycle represents a major anaplerotic step in Gln metabolism. To examine the impact of elevated  $\alpha$ -KG levels on the reproductive phenotypes of female mice, dimethyl- $\alpha$ -ketoglutarate (DM- $\alpha$ KG), a cell-permeable form of  $\alpha$ -KG, was injected intraperitoneally into 3-week-old C57BL/6 mice (designated as DM- $\alpha$ KG mice) (Fig. 6j). The ovarian volume was reduced in DM- $\alpha$ KG mice compared to controls (Supplementary Fig. 4i). An analysis of follicular development at different stages revealed an increased number of primary follicles and a reduced number of secondary follicles and antral follicles in the ovaries of DM- $\alpha$ KG mice, while the numbers of primordial follicles and corpus lutea did not differ between the two groups (Fig. 6k). Furthermore, DM- $\alpha$ KG mice exhibited irregular estrous cycles (Fig. 6l, m). Taken together, these data indicated the excessive  $\alpha$ -KG accumulation via *SLC1A5*-mediated Gln uptake in GCs, leading to a PCOS-like phenotype and impaired follicle development in mice.

### H3K14ac and H3K56ac mediate HDAC5 and $\alpha$ -KG action regarding *CYP19A1* expression

Since the accumulation of  $\alpha$ -KG is a crucial intermediate step, we further focused on how the  $\alpha$ -KG accumulation leads to the development of PCOS. Since DM- $\alpha$ KG mice exhibited PCOS-like traits, we performed RNA-seq analysis on DM- $\alpha$ KG-treated KGN cells. Our transcriptomic profiling revealed 1582 differentially expressed genes (DEGs), with 1093 upregulated and 489 downregulated genes (Supplementary Fig. 5a). A substantial fraction of genes was enriched in the metabolism of steroids, regulation of cholesterol biosynthesis, and chromosome maintenance pathways (Fig. 7a). Moreover, GSEA revealed significant enrichment in steroid metabolism, PCOS, and post-translational protein modification pathways (Supplementary Fig. 5b-d).

Histone post-translational modifications (HPTMs) participate in local compaction during chromosome condensation<sup>28</sup>. We first evaluated various histone methylation modifications given their previously reported involvement in  $\alpha$ -KG regulation<sup>29,30</sup>. Surprisingly, we did not observe significantly consistent changes between DM- $\alpha$ KG-treated and OE-*SLC1A5* KGN cells in histone methylation modifications (Supplementary Fig. 5e-g). While H3K4me1 and H3K4me3 showed a downward trend in the DM- $\alpha$ KG-treated group, these reductions lacked statistical significance (Supplementary Fig. 5f). Furthermore, no significant differences of H3K4me1 and H3K4me3 were observed in *SLC1A5*-overexpressing cells (Supplementary Fig. 5g). Similarly, H3K9me2 displayed significant downregulation exclusively in *SLC1A5*-overexpressing KGN cells (Supplementary Fig. 5g), with no comparable changes in the DM- $\alpha$ KG-treated group.

On the other hand, we found the downregulation of histone 3 lysine 14 acetylation (H3K14ac) and histone 3 lysine 56 acetylation (H3K56ac) exhibited consistent results under the regulation of either *SLC1A5* overexpression or  $\alpha$ -KG accumulation (Fig. 7b, Supplementary Fig. 5h, i). To explore the reasons behind the changes in histone acetylation levels, we performed RNA-seq analysis on OE-*SLC1A5* KGN cells and found the mRNA expression levels of histone deacetylase 5 (*HDAC5*) were significantly elevated (Fig. 7c). *HDAC5* belongs to the class IIa family of HDACs and regulates gene expression by deacetylating lysine residues in histone tails and facilitating chromatin remodeling<sup>31</sup>. We further validated the increase in *HDAC5* expression at the protein level (Fig. 7d, Supplementary Fig. 6a). Moreover, the elevated mRNA expression level of *HDAC5* was also observed in HA-PCOS patients (Supplementary Fig. 6b). To elucidate the impact of  $\alpha$ -KG accumulation on *HDAC5* expression, we treated KGN cells with DM- $\alpha$ KG and observed a substantial increase in *HDAC5* protein levels (Fig. 7e, Supplementary Fig. 6c), suggesting that *SLC1A5* enhances *HDAC5* expression through  $\alpha$ -KG accumulation. Additionally, *HDAC5* overexpression resulted in decreased levels of H3K14ac and H3K56ac (Fig. 7f, Supplementary Fig. 6d).

It is known that the decrease in H3K14ac and H3K56ac levels is associated with gene repression<sup>32-35</sup>. Thus, we performed a combined analysis of downregulated genes influenced by *HDAC5* and DM- $\alpha$ KG. Interestingly, we found several steroid synthesis and PCOS-related genes, including *CYP19A1* among intersecting genes (Fig. 7g). The *CYP19A1* gene, located on chromosome 15q21.1, encodes aromatase (P450arom), an essential steroidogenic enzyme that catalyzes the final steps of estrogen biosynthesis<sup>36</sup>. This enzyme converts TT and androstenedione into E2 and estrone, respectively, in both gonadal and extragonadal tissues<sup>37</sup>. The mRNA levels of *CYP19A1* declined in a time-dependent manner following DM- $\alpha$ KG treatment and *SLC1A5* or *HDAC5* overexpression (Fig. 7h, i). Furthermore, *CYP19A1* was downregulated at both the mRNA and protein levels in GCs from HA-PCOS patients (Fig. 7j-l).

We further performed CUT & Tag analysis (Supplementary Fig. 7a, b). The results revealed substantially decreased levels of H3K14ac and H3K56ac at the promoter and enhancer regions of *CYP19A1* in DM- $\alpha$ KG-induced KGN cells (Fig. 7m), as well as 7-dehydrocholesterol reductase (*DHCR7*), transmembrane 4L 6 family member 4 (*TM4SF4*), 24-dehydrocholesterol reductase (*DHCR24*), endothelin 2 (*EDN2*), insulin induced gene 1 (*INSIG1*), follistatin (*FST*), homo sapiens 3-hydroxy-3-methylglutaryl-CoA synthase 1 (*HMGCS1*) and fatty acid desaturase 2 (*FADS2*) (Supplementary Fig. 7c-j). Furthermore, to further clarify the potential role of histone methylation, we then supplemented CUT & Tag experiments to provide a detailed analysis of histone methylation, specifically H3K4me1, H3K4me3, and H3K9me2, under both *SLC1A5*-overexpressing and DM- $\alpha$ KG-treated conditions. Based on good data quality (Supplementary Fig. 8a), the results of CUT & Tag revealed that for the overlapping genes identified by RNA-seq, including *CYP19A1*, *DHCR7*, *DHCR24*, *INSIG1*, *HMGCS1*, *TM4SF4*, *EDN2*, *FST*, and *FADS2*, the differences in peaks at their promoter regions are not significant (Supplementary Fig. 8b-j).

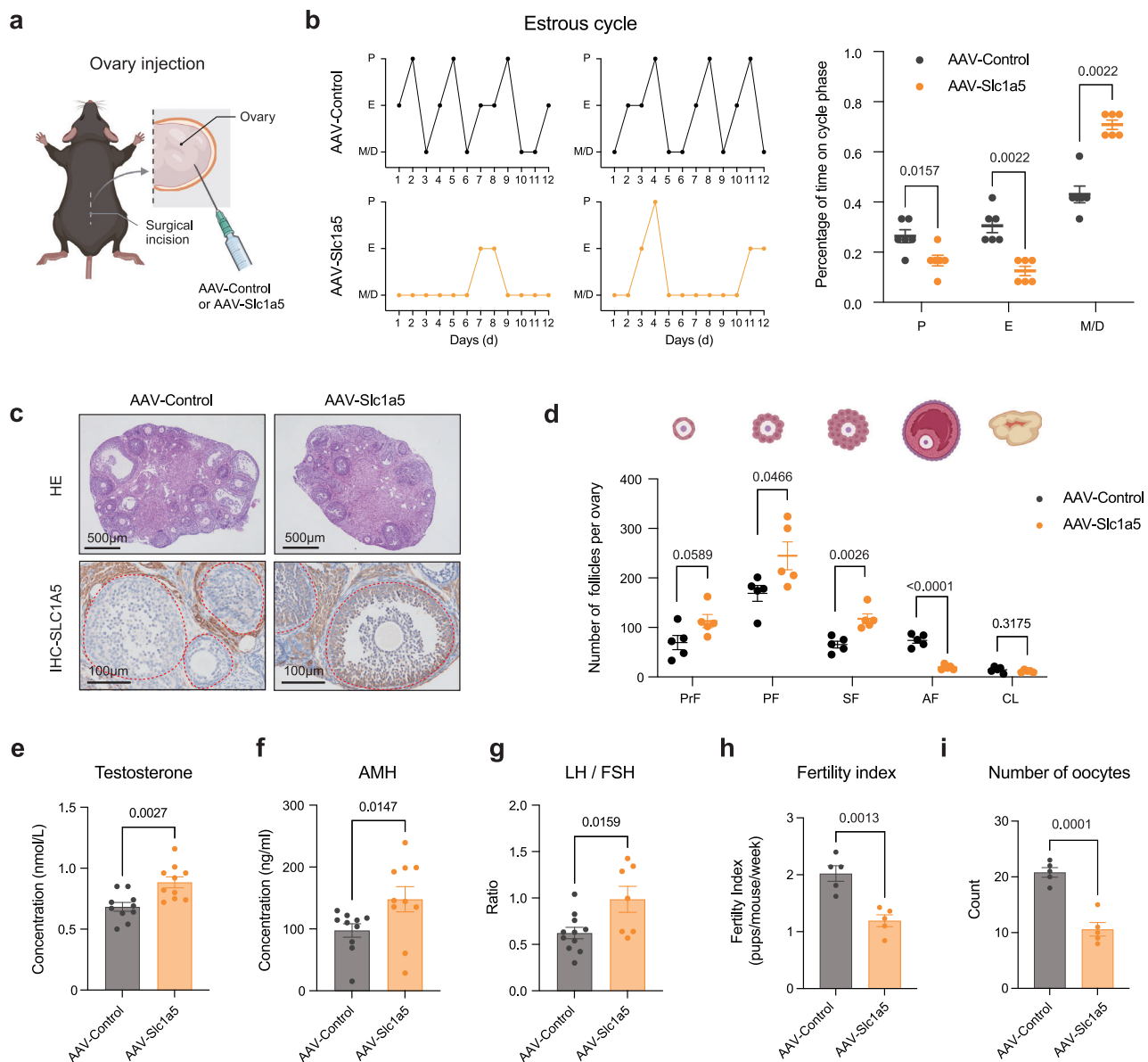


**Fig. 3 | SLC1A5 overexpression in mouse ovaries induces PCOS-like traits and impairs follicle development.** **a** Schematic diagram of mouse ovarian orthotopic injection surgery. Created in BioRender. Ye, L. (2025) <https://BioRender.com/bpgxw4/>. **b** Estrous cycle monitoring in AAV-Control and AAV-Slc1a5 mice was conducted over 2 weeks using vaginal cytology ( $n = 6$  for each group). P, proestrus; E, estrus; M/D, metestrus/diestrus phase. **c** Representative images of ovarian HE staining and immunohistochemistry (IHC) staining of SLC1A5 showing follicular development in AAV-Control and AAV-Slc1a5 mice (scale bar: 500  $\mu\text{m}$  and 100  $\mu\text{m}$ ). The experiment was repeated three times independently with similar results. **d** Follicle number of primordial (PrF), primary (PF), secondary (SF), antral follicles

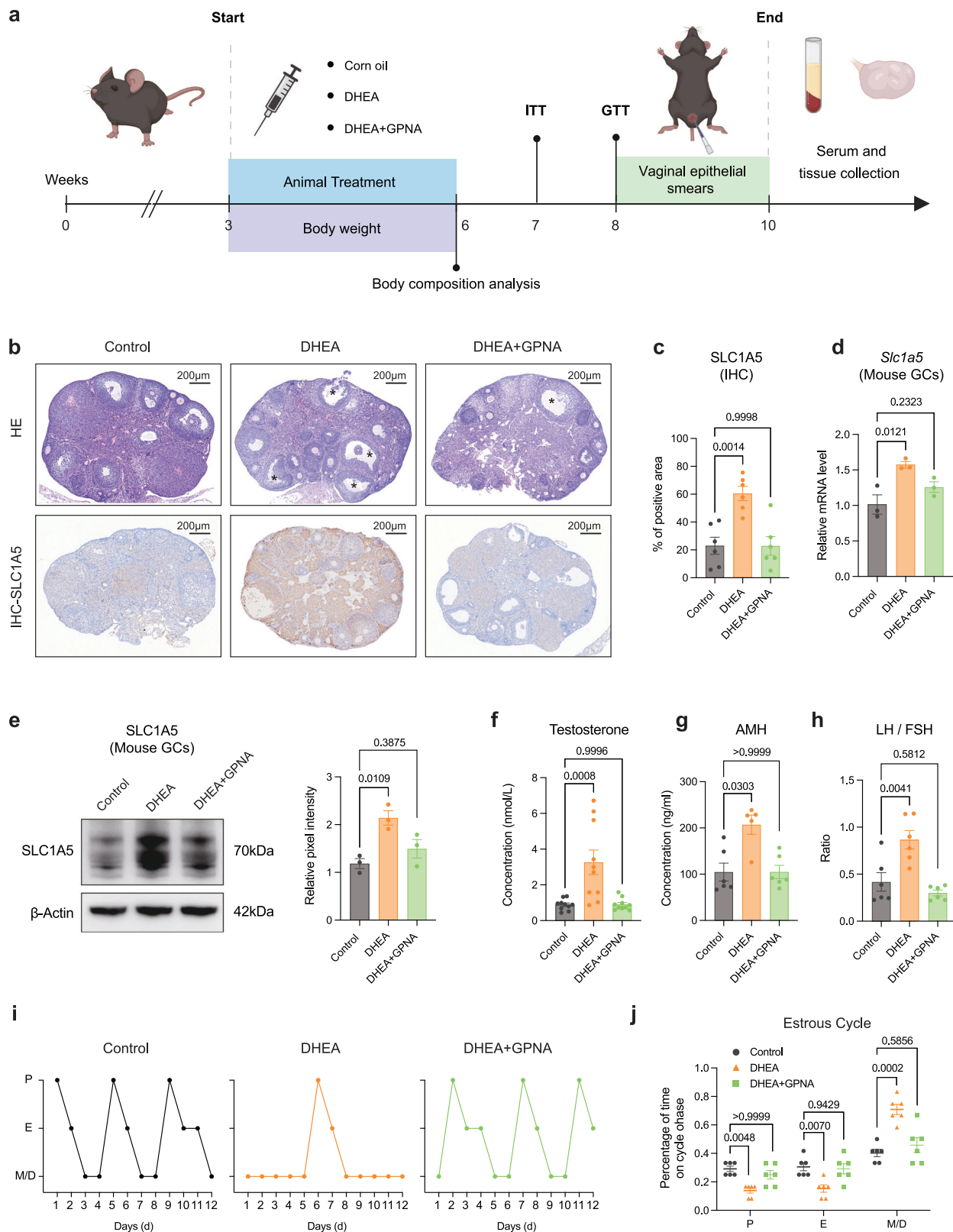
(AF), and corpus luteum (CL) in HE-stained ovarian sections of AAV-Control and AAV-Slc1a5 mice ( $n = 5$  for each group). **e** Serum levels of TT measured using LC-MS ( $n = 10$  for each group). **f** Serum AMH levels measured using ELISA ( $n = 10$  for each group). **g** Serum LH/FSH ratio measured using ELISA (AAV-Control  $n = 11$ , AAV-Slc1a5  $n = 7$ ). **h** Fertility index calculated through reproductive experiments ( $n = 5$  for each group). **i** Number of oocytes counted after superovulation ( $n = 5$  for each group). Statistical analyses were performed using the Student's *t* test or the Mann-Whitney test in (**b**, **d**, **e–i**). Data are presented as the mean  $\pm$  SEM. All tests were two-sided. The biological replicates are used for statistical analysis in (**b**, **d**, **e–i**). Source data are provided as a Source Data file.

To validate these findings *in vivo*, we took advantage of the prepubertal DHEA-induced PCOS mice (Fig. 8a). The results showed that both *Slc1a5* and *Hdac5* mRNA levels and their protein levels (SLC1A5 and HDAC5) were significantly elevated, whereas *Cyp19a1* mRNA and CYP19A1 protein levels decreased notably in the ovaries of DHEA-induced mice (Fig. 8b–h). Similar patterns were observed in prenatal anti-Müllerian hormone (PAMH) model (Fig. 8i). In the ovaries of PAMH mice, we also detected higher levels of Gln (Fig. 8j). Moreover, we observed increased mRNA levels and protein levels of SLC1A5 and HDAC5 while decreased mRNA levels and protein levels of CYP19A1 in their ovaries

(Fig. 8k–q), consistent with the proposed mechanism of glutamine metabolism reprogramming and epigenetic regulation.

## Discussion

Despite decades of research into the pathology of PCOS, the mechanisms by which dysregulation of amino acid metabolism contributes to its development remain unclear. In this study, we collected FF and GC samples from patients with PCOS to profile amino acids uptake and assess the expression of metabolic-related genes in GCs. This study provided significant insights into the complex relationship between Gln metabolism reprogramming in GCs and



hyperandrogenism in women with PCOS, highlighting potential metabolic dysregulation of Gln uptake underlying this condition.

In comparison to control ovaries, tissue from anovulatory women with polycystic ovaries exhibited a higher proportion of increased GC division, highlighting the abnormal dynamics of early follicle development<sup>38</sup>. Notably, androgens enhance the proliferation of GCs and progressively increase the number and thickness of the

thecal layer in growing preantral and small antral follicles, providing a plausible explanation for anovulation in PCOS<sup>39</sup>. Rapidly dividing cells are likely to utilize Gln for energy production as well as a source of carbon and nitrogen for biomass accumulation<sup>40</sup>. The rapid growth of GCs resembles the tumorigenic potential observed in early-stage follicles, suggesting that Gln uptake may be upregulated in PCOS to fulfill nutrient demands. Our comprehensive assessments

**Fig. 4 | SLC1A5 inhibitor, GPNA, confers reproductive benefits to PCOS-like mice.** **a** Schematic diagram of PCOS-like mouse modeling and tissue collection. Created in BioRender. Ye, L. (2025) <https://BioRender.com/z45m452>. **b** Representative images of ovarian HE staining and IHC staining of SLC1A5 showing follicular development in Control, DHEA, and DHEA + GPNA mice (scale bar: 200  $\mu$ m). The experiment was repeated three times independently with similar results. **c** Percentage of SLC1A5 positive area determined by IHC ( $n = 6$  for each group). **d** mRNA expression of *Slc1a5* in the mouse GCs determined by qPCR ( $n = 3$  for each group). **e** Western blot analysis of SLC1A5 in mouse GCs ( $n = 3$  for each group).  $\beta$ -Actin was denoted as an internal reference protein. **f** Serum levels of TT measured

using LC-MS ( $n = 10$  for each group). **g** Serum levels of AMH measured using ELISA (Control  $n = 6$ , DHEA  $n = 5$ , DHEA + GPNA  $n = 6$ ). **h** Serum levels of LH/FSH ratio measured using ELISA ( $n = 6$  for each group). **i, j** Estrous cycle monitoring conducted over 2 weeks using vaginal cytology (**i**) and percentage of time on cycle phase (**j**) in Control, DHEA and DHEA + GPNA mice was ( $n = 6$  for each group). For statistical analysis, one-way ANOVA followed by Tukey's multiple comparisons test or Kruskal-Wallis test with Dunn's test was utilized. Data are presented as the mean  $\pm$  SEM. All tests were two-sided. The biological replicates are used for statistical analysis in (**c–h, j**). Source data are provided as a Source Data file.

revealed a strong relationship between excess androgen and increased Gln uptake.

Gln serves several essential roles in follicular development. Evidence indicates that LH stimulates Gln metabolism in intact cumulus cell-enclosed oocytes<sup>41</sup>. Before ovulation, the rapid decline in FSH levels leads to decreased Gln concentrations, facilitating the breakdown of the follicle wall necessary for ovulation<sup>16</sup>. Additionally, traits associated with PCOS correlate with dysregulated Gln metabolism. Both dysregulated androgen signaling<sup>19</sup> and insulin signaling<sup>42</sup> enhance Gln uptake. Previous studies have shown that abnormally high levels of FSH in the FF of patients with PCOS upregulate the Gln synthetase (GS) expression in GCs, thereby increasing Gln synthesis and its secretion into the FF<sup>16</sup>. These findings partially align with our results; we observed elevated Gln levels in GCs of women with PCOS, but results concerning FF remain inconsistent. The resolution to this paradox likely lies in the balance between the absorption and secretion capacities at various stages of follicle development. Zhang et al. focused on the pre-ovulation stage during which FSH influences Gln secretion. However, the significant influence of androgen was neglected, which is widely recognized as a primary contributor to anovulation in PCOS. By carefully stratifying androgen levels, we propose that the abnormal function of antral follicles may stem from increased Gln uptake during earlier stages of preantral follicle development. Moreover, insufficient FSH levels, as opposed to elevated levels, are believed to hinder follicular development in PCOS. Additionally, the low to normal serum concentrations of FSH in many PCOS patients restrict its ability to regulate GS synthesis<sup>36</sup>. Our findings support the hypothesis that hyperandrogenism is a key factor in PCOS and further clarify the role of abnormal Gln metabolism in its development.

While reduced ROS is generally considered beneficial, the maintenance of ROS homeostasis is more critical for cellular health. Ovulation requires a breakdown of the follicle wall, which can be achieved through apoptosis of GCs. It has been reported that GCs from PCOS patients exhibit a lower apoptotic rate<sup>43</sup>. In our study, we observed reduced ROS levels in SLC1A5-overexpressing KGNs, which may impair proper apoptotic processes, potentially contributing to ovulatory dysfunction in PCOS.

In recent years, considerable attention has been directed towards epigenetic factors in the study of PCOS<sup>5,35,37,44</sup>. The establishment of epigenetic signatures is mediated by specific enzymes, whose activity relies on the direct sensing of intermediary metabolites<sup>38,39,41,45</sup>. For instance, ten-eleven translocation (Tet) enzymes and JmjC domain-containing histone demethylases require  $\alpha$ -KG for their activity, whereas histone acetyltransferases (HATs) rely on intracellular acetyl-CoA levels<sup>30,46</sup>. Our study revealed that overexpression of SLC1A5 resulted in an accumulation of  $\alpha$ -KG derived from activated glutaminolysis.

When investigating the impact of the SLC1A5- $\alpha$ KG axis on histone modification changes, we first examined alterations in histone methylation. However, no consistent modifications were observed in either SLC1A5-overexpressing groups or DM- $\alpha$ KG-treated groups. Subsequently, we shifted our focus to histone acetylation and identified a consistent downregulation of H3K14ac and H3K56ac. While acetylation changes appear more prominent, we fully acknowledge that histone methylation modifications might still contribute to PCOS

epigenetics. Further research is needed to elucidate the role of  $\alpha$ -KG in regulating histone modification interplay.

Subsequently, we characterized several steroid biosynthetic genes, including *CYP19A1*, by examining the genes downregulated in both HDAC5-overexpressing and DM- $\alpha$ KG-treated KGN cells. Low levels of aromatase, encoded by *CYP19A1*, have been observed in GCs derived from medium-sized follicles in women with PCOS<sup>47,48</sup>. Furthermore, several studies have reported an association between the single-nucleotide polymorphisms (SNPs) rs2414096 of the *CYP19A1* gene and elevated androgen concentrations in women with PCOS<sup>36,46,49–51</sup>.

This current study has several limitations. First, the conditional knock-in mouse model would strengthen the evidence for SLC1A5's functional role in PCOS pathogenesis. Second, the specific mechanism underlying  $\alpha$ -KG selective modulation of histone acetylation, rather than methylation, remains to be elucidated. It remains elusive why  $\alpha$ -KG alters histone acetylation rather than methylation levels. Although our data suggest HDAC5 as a potential mediator of  $\alpha$ -KG's effects, the precise molecular mechanisms require further exploration. One possibility is that  $\alpha$ -KG alters the chromatin accessibility of *HDAC5* promoter regions via DNA demethylation or histone methylation. Further investigation should be involved to determine whether other HDACs, sirtuins, or ubiquitin ligases contribute to SLC1A5-mediated amino acid metabolism and follicle arrest.

In conclusion, this study demonstrated that cells have developed aberrant "sensing" mechanisms to detect hormone fluctuations and adjust their transcriptional programs via epigenetic modifications, exacerbating hormonal homeostasis imbalance (Fig. 9). Moreover, the dysregulation of the SLC1A5- $\alpha$ -KG-histone acetylation axis negatively impacted E2 production. Overexpression of *Slc1a5* in female mice resulted in phenotypes similar to estrogen receptor-knockout females, including follicle development arrest and impaired fertility<sup>16,52</sup>. Overall, we identify aberrant Gln uptake as a crucial factor in the development of PCOS and highlight SLC1A5 as a promising therapeutic target. These findings provide important insights into the metabolic and epigenetic mechanisms underlying PCOS, as well as potential pathways for the development of more effective therapeutic interventions.

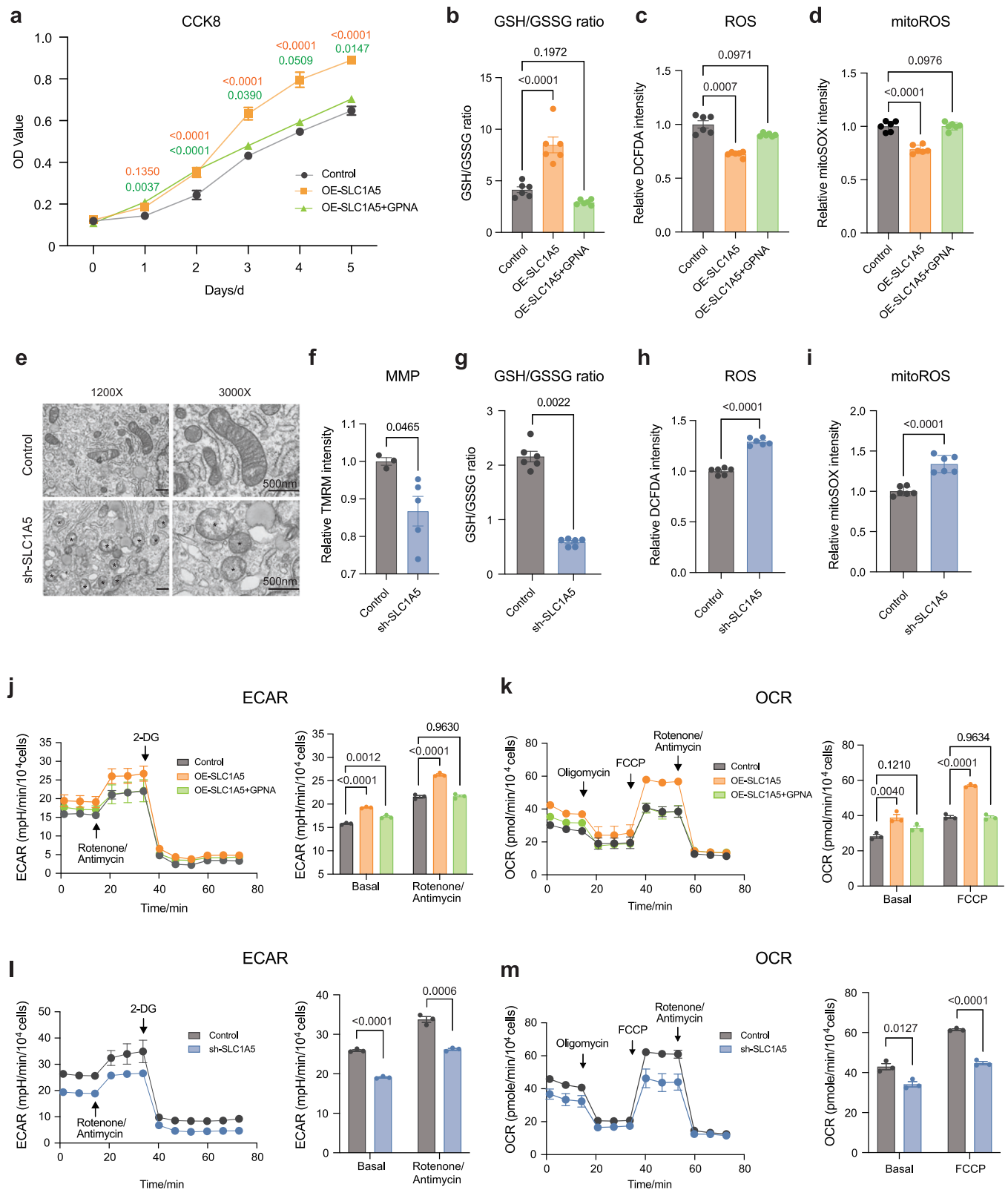
## Methods

### Ethical statement

This study was approved by the Ethics Committee of the International Peace Maternity and Child Health Hospital, School of Medicine, Shanghai Jiao Tong University on 2 August 2016 (Approval Number: GKLW 2015-42). Informed was obtained from all participants before inclusion in the study.

### Study populations

A total of 65 Chinese Han women were enrolled from outpatients who sought assisted reproduction technology (ART) treatment at the Reproductive Medicine Center, International Peace Maternity and Child Health Hospital, School of Medicine, Shanghai Jiao Tong University. This study included 43 women diagnosed with PCOS and 22 healthy women as controls. PCOS diagnosis was established according to the 2003 Rotterdam criteria, requiring at least two of the following



features after exclusion of other etiologies: oligo-ovulation or anovulation; clinical or biochemical hyperandrogenism; polycystic ovarian morphology on ultrasound. The hyperandrogenic group was defined by serum TT levels exceeding 0.69 ng/mL. The control subjects were supposed to have regular menstrual cycles and normal ovarian morphology without clinical or biochemical hyperandrogenism. The exclusion criteria for differentiating both PCOS and control patients

include: 1) age > 35 years; 2) chromosomal abnormalities; 3) premature ovarian failure, endometriosis, gynecological tumors (such as ovarian tumors, endometrial tumors as well as cervical cancer), and any ovarian surgery; 4) endocrine disorders; 5) serious and unstable diseases (cardiovascular, liver, and kidney diseases, etc.); 6) history of failed in vitro fertilization cycles more than three times; 7) use of medications known to affect metabolic function or reproductive

**Fig. 5 | SLC1A5 mediates energy metabolism and drives  $\alpha$ -KG accumulation.** a Cell Counting Kit-8 (CCK8) assays performed in the Control ( $n = 3$ ), OE-SLC1A5 ( $n = 3$ ) and OE-SLC1A5 + GPNA ( $n = 5$ ) KGN cells. Orange figures denote significant differences between Control and OE-SLC1A5, and green figures denote significant differences between Control and OE-SLC1A5 + GPNA. **b–d** GSH/GSSG ratio (**b**), ROS (**c**), and mitoROS (**d**) in Control, OE-SLC1A5, and OE-SLC1A5 + GPNA KGN cells ( $n = 6$  for each group). GSH, glutathione; GSSG, oxidized glutathione; ROS, reactive oxygen species. **e** Transmission electron microscope (TEM) of mitochondria in Control and sh-SLC1A5 cells. (\*indicates damaged mitochondria, Scale bar = 500 nm). The experiment was repeated three times independently with similar results. **f** Mitochondrial membrane potential (MMP) in Control ( $n = 3$ ) and sh-SLC1A5 KGN ( $n = 5$ ) cells measured by flow cytometry. **g–i** GSH/GSSG ratio (**g**), ROS

(**h**), and mitoROS (**i**) detected in Control and sh-SLC1A5 KGN cells ( $n = 6$  for each group). **j, k** Extracellular acidification rates (ECARs) (**j**) and oxygen consumption rates (OCRs) (**k**) were assessed in Control, OE-SLC1A5, and OE-SLC1A5 + GPNA KGN cells ( $n = 3$  for each group). **l, m** ECARs (**l**) and OCRs (**m**) were assessed in Control, sh-SLC1A5 KGN cells ( $n = 3$ ). For statistical analysis, two way ANOVA followed by Tukey's multiple comparisons tests was applied to (**a**); one-way ANOVA followed by Tukey's multiple comparisons tests was performed in (**b, d, j, k**); Welch's ANOVA followed by Dunnett's T3 multiple comparisons test was performed in **c**; Student's *t* tests were performed in (**f, h, i, l, m**) and a Mann-Whitney test was performed in (**g**). Data are presented as the mean  $\pm$  SEM. All tests were two-sided. Source data are provided as a Source Data file.

function within 3 months before enrolment. Written informed consent has been obtained from the human subjects involved in the study.

### Collection of follicular fluid and luteinized granulosa cells samples

The FF samples and luteinized GCs were collected from the first aspirated ovarian follicle with a diameter of 16–18 mm at the time of oocyte retrieval. The aspirated fluid was centrifuged at 20 min, 1000 $\times$ g, and the resulting supernatant was aliquoted into 2 ml EP tubes as FF samples. The pellets were resuspended in phosphate-buffered saline (PBS) containing 0.1% hyaluronidase (Sigma-Aldrich, MO, USA) at 37 °C for 20 min. GCs were further purified using Ficoll-Paque (GE Healthcare, Uppsala, Sweden) density gradient centrifugation. The samples were stored at –80 °C for later analysis.

### Serum hormone analysis

The levels of day 3 serum hormones were measured at the International Peace Maternity and Child Health Hospital, School of Medicine, Shanghai Jiao Tong University. Briefly, serum LH, FSH, prolactin (PRL), E2, and P were analyzed by chemiluminescence immunoassays (CLIA), and AMH levels were measured by ELISA. For the measurement of TT, we determined TT levels in a subset of samples by LC-MS and established a standard calibration curve by correlating these measurements with the original CLIA-derived TT concentrations. The final TT concentrations of all participants were calculated through a standard curve. The intra-assay coefficient of variation (CV) was 3.6 % for LH, 3.1 % for FSH, 1.42 % for PRL, 12 % for E2, 6.11 % for P, 1.67 % for T, and 8.00 % for AMH.

### Animal studies

Animal experiments were conducted under the Guide for the Care and Use of Laboratory Animals at Shanghai Jiao Tong University (Approval ID: A2023180-001). All mice were maintained under specific pathogen-free (SPF) conditions at 24 °C with 40–70% relative humidity and a 12-h light/dark cycle. Animals were housed five per cage with ad libitum access to water and chow (Shanghai Slac Laboratory Animal Co., Ltd, P1300F-25). All procedures were designed to minimize animal suffering and were approved by the Institutional Animal Care and Use Committee.

### In situ injection of AAV into mouse ovaries

The mouse AAV-SLC1A5 vector was constructed by Obio Technology Corp., Ltd. (Shanghai, China). Four-week-old female C57BL/6J mice were anesthetized using isoflurane. Anesthesia was maintained throughout the procedure, and the depth of anesthesia was monitored by assessing the toe pinch reflex and respiration rate. The abdominal cavity was accessed via a midline incision, and the ovaries were carefully exposed. A microinjector was used to deliver 4  $\mu$ L of AAV (with a titer of  $1 \times 10^{13}$  vg/mL) directly into each ovary. After injection, the incision was closed using sutures and adhesive. Mice were monitored post-surgery for recovery and any signs of distress. Experiments or tissue collection were initiated starting from the third week after viral injection.

### PCOS-like mouse model

Female C57BL/6J mice were purchased from Shanghai Lingchang Biotechnology Co., Ltd (Shanghai, China) and randomly assigned to three experimental groups based on body weight. The control group received daily subcutaneous injections of corn oil (10  $\mu$ L/g body weight, Med Chem Express, NJ, USA) for 21 consecutive days. The PCOS-like model group (DHEA group) was induced by daily subcutaneous injections of DHEA (Med Chem Express) dissolved in corn oil (600 mg/kg body weight) for 21 consecutive days. The inhibitor treatment group (DHEA + GPNA group) received daily subcutaneous injections of DHEA (600 mg/kg body weight) along with intraperitoneal injections of the inhibitor GPNA (200 mg/kg body weight, Selleck, TX, USA) every other day for 21 consecutive days. All experimental treatments were initiated when mice reached 3 weeks of age and were maintained for 21 consecutive days. Body weight was monitored daily throughout the study period to ensure precise dose calculations.

### DM- $\alpha$ KG mouse model

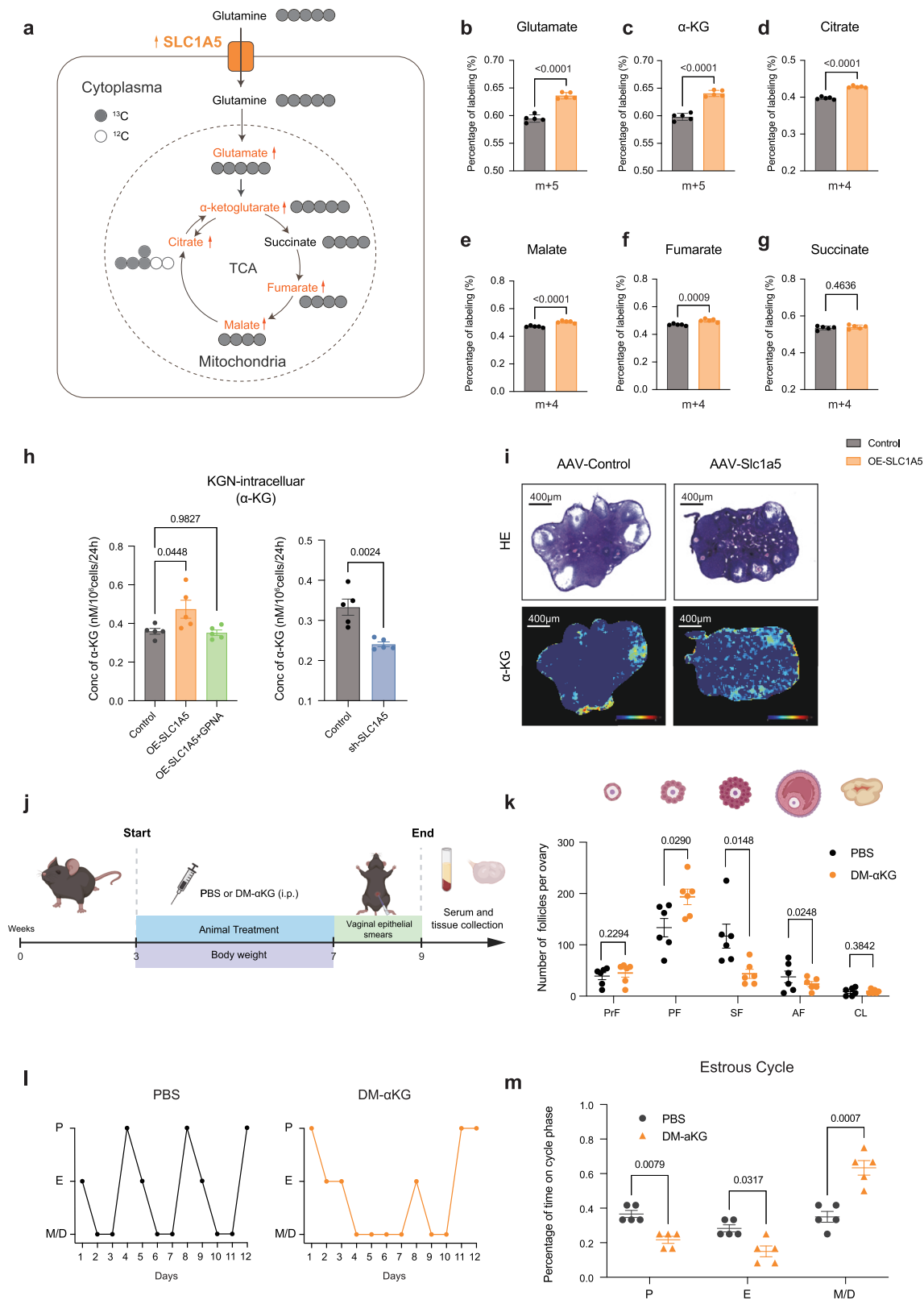
Female C57BL/6J mice were purchased from Shanghai Lingchang Biotechnology Co., Ltd (Shanghai, China) and randomly assigned to two experimental groups based on body weight. The control group (PBS group) received intraperitoneal injections of PBS (10  $\mu$ L/g body weight) every other day for 28 consecutive days. The treatment of the dimethyl- $\alpha$ -ketoglutarate group (DM- $\alpha$ KG group) was administered intraperitoneal injections of 600 mg/kg DM- $\alpha$ KG (Sigma-Aldrich, 349631) every other day for 28 consecutive days. All interventions were initiated in 3-week-old mice and continued for 28 days, with periodic body weight monitoring to ensure accurate dose administration.

### Prenatal anti-Müllerian hormone (PAMH) model

The PAMH animal model was established following published protocols<sup>53</sup>. Female C57BL6/J dam at 3–4 months received daily intraperitoneal injections between embryonic days 16.5 and 18.5. The control group received intraperitoneal injections of PBS (10  $\mu$ L/g body weight), while the PAMH group was administered AMH (0.12 mg/kg body weight, R&D Systems, 1737-MS-010, MN, USA) via intraperitoneal injection.

### Targeted Metabonomic Analysis

The metabonomic analysis for FF (Control  $n = 22$ , NA-PCOS  $n = 21$ , HA-PCOS  $n = 22$ ) and KGN cells (Control  $n = 6$ , DHT  $n = 6$ , OE-SLC1A5  $n = 6$ ) was conducted by a gas chromatography-mass spectrometry (GC-MS) system. FF (500  $\mu$ L) was mixed with methanol-acetonitrile (400  $\mu$ L, v/v = 2:1, with formic acid and succinic acid-2,2,3,3-d4), and KGN cells ( $1 \times 10^7$ ) were treated with methanol-water (v/v = 3:1, with 0.1% formic acid and succinic acid-2,2,3,3-d4), respectively. The samples were then sonicated and centrifuged at 10,000 $\times$ g for 10 min. After centrifugation, the supernatant was transferred to a new EP tube and dried, followed by derivatization reagent treatment. Then, the samples were subjected to GC-MS analysis. A TSQ9000 GC-MS/MS system (Thermo Scientific, MA, USA) was used to perform metabolite identification and quantification. GC analysis utilized a DB-5MS capillary column (30 m  $\times$  0.25 mm  $\times$  0.25  $\mu$ m, Agilent J&W Scientific, CA, USA) with high-purity



helium ( $\geq 99.999\%$ ) at 1.2 mL/min. MS used an electron ionization (EI) source (300 °C), transfer line (280 °C), and selected reaction monitoring (SRM) mode ( $m/z$  40–600). Data were processed with TraceFinder software (v4.1, Thermo Scientific). FF sample concentrations were calculated as  $(C \times V1) / M$ , where C is the concentration from the standard curve, V1 is which is the volume of the solution after dilution (0.5 ml), and M is the sample amount. KGN sample concentrations

were determined as  $C / NI$ , where C is the concentration from the standard curve and NI is the protein concentration measured by BCA assay.

For clinical GCs (Control  $n = 14$ , NA-PCOS  $n = 13$ , HA-PCOS  $n = 13$ ), the metabolomic analysis was conducted by the liquid chromatography-mass spectrometry (LC-MS) system. The cell pellet was resuspended in 100  $\mu$ L of extraction solution. Cell suspension

**Fig. 6 |  $\alpha$ -KG treatment induces PCOS-like traits.** **a** Schematic diagram of Gln metabolism in cytoplasm and mitochondria with L-Gln ( $^{13}\text{C}_5$ , 99%) as a tracer. **b–g** Labeling patterns of glutamate (**b**),  $\alpha$ -KG (**c**), citrate (**d**), malate (**e**), fumarate (**f**), and succinate (**g**) from L-Gln ( $^{13}\text{C}_5$ , 99%) in Control, OE-SLC1A5, and OE-SLC1A5 + GPNA KGN cells ( $n = 5$  for each group).  $m + n$  represents the total fraction of a compound, where  $m$  is the natural isotope fraction and  $n$  is the number of  $^{13}\text{C}$  atoms. **h** The intracellular  $\alpha$ -KG levels in Control, OE-SLC1A5, OE-SLC1A5 + GPNA, and sh-SLC1A5 KGN cells ( $n = 5$  for each group). **i** Representative images of HE staining and MALDI mass spectrometry imaging of  $\alpha$ -KG on murine ovaries (scale bar: 400  $\mu\text{m}$ ). The experiment was repeated three times independently with similar results. **j** Schematic

diagram of DM- $\alpha$ KG injection-induced mouse modeling. Created in BioRender. Ye, L. (2025) <https://BioRender.com/w83x073>. **k** Follicle number of primordial (PrF), primary (PF), secondary (SF), antral follicles (AF), and corpus luteum (CL) performed on HE-stained ovarian sections in PBS and DM- $\alpha$ KG mice ( $n = 6$  for each group). **l, m** Estrous cycle monitoring and conducted over 2 weeks using vaginal cytology (**l**) and percentage of time on cycle phase (**m**) in PBS and DM- $\alpha$ KG mice ( $n = 5$  for each group). For statistical analysis, Student's *t* tests and Mann-Whitney tests were performed in (**b–g**, **h**, **k**, **m**); and one-way ANOVA followed by Tukey's multiple comparisons test was performed in (**h**). Data are presented as the mean  $\pm$  SEM. All tests were two-sided. Source data are provided as a Source Data file.

(50  $\mu\text{L}$ ) was rapidly frozen in liquid nitrogen and thawed three times with a mixture of methanol (200  $\mu\text{L}$ ). The sample was centrifuged at 10,000 $\times g$  for 10 min, and 200  $\mu\text{L}$  of the supernatant was filtered through a protein precipitation plate. Metabolite analysis utilized an ExionLC AD (SCIEX, MA, USA) and QTRAP 5500 LC-MS/MS system (SCIEX). Chromatography was performed on an ACQUITY BEH Amide column (1.8  $\mu\text{m}$ , 2.1 mm  $\times$  100 mm; Waters) with a gradient of ultrapure water and acetonitrile (both containing ammonium acetate and formic acid), at 0.4 mL/min, 40  $^\circ\text{C}$ , and 2  $\mu\text{L}$  injection volume. MS operated in EI mode with a 550  $^\circ\text{C}$  source temperature, voltages of 5500 V (positive ions) and 4500 V (negative ions). Data acquisition and analysis were performed using Analyst software (SCIEX). GC concentrations were calculated as  $C/\text{NI}$ , where  $C$  is the concentration from the standard curve and  $\text{NI}$  is the protein concentration measured by the BCA assay.

### MALDI mass spectrometry imaging

Frozen mouse tissues were cryosectioned into 10  $\mu\text{m}$  (Leica, Wetzlar, Germany) and thaw mounted onto indium tin oxide (ITO)-coated microscope slides (Bruker, Bremen, Germany). A solution of 2,5-dihydroxybenzoic acid (DHT) was prepared in 90% methanol with 0.3% trifluoroacetic acid (TFA). For cell metabolite imaging, the sections were coated with a solution of DHT TM-sprayer (HTX Technologies, NC, USA). The TM-sprayer parameters were set as follows: spray nozzle velocity, 1200 mm/min; track spacing, 2 mm; flow rate, 0.12 mL/min; spray nozzle temperature, 72  $^\circ\text{C}$ ; and nitrogen gas pressure, 10 psi. MALDI mass spectrometry imaging (MSI) was performed in positive mode on tims TOF flex MALDI 2 (Bruker). Full-scan images were collected for a mass range of 50–650  $m/z$ , with a pixel size of 50  $\mu\text{m} \times 50 \mu\text{m}$ . The frequency of the laser was set to 10,000 Hz, with 70% of the laser energy and 200 laser shots per pixel. SCI LS Lab software (version 2021c premium, Bruker) was used to analyze the MSI data.

### Assessment of reproductive phenotypes

Vaginal cells were collected daily from the mice using normal saline lavage for 12 consecutive days. The estrous cycle phase was determined based on the presence or absence of leukocytes, cornified epithelial cells, and nucleated epithelial cells.

For serum hormone assays, mice were anesthetized, and blood was collected via cardiac puncture. Serum and blood cells were separated by centrifugation. Quantification of serum TT was carried out using the previously reported method<sup>54,55</sup>, with some modifications. In brief, 50  $\mu\text{L}$  serum was added with 10  $\mu\text{L}$  of testosterone- $\text{d}_3$ , 500  $\mu\text{L}$  precooled aqueous methanol (4:1, v/v), vortexed for 1 min, and centrifuged (14,000 $\times g$ , 4  $^\circ\text{C}$ ) for 15 min to obtain 400  $\mu\text{L}$  supernatant. After repeating the extraction, combined supernatants (800  $\mu\text{L}$ ) were nitrogen-dried and reconstituted in 50  $\mu\text{L}$  methanol/water (1:1, v/v). The residues were reconstituted in 50  $\mu\text{L}$  aqueous methanol (1:1, v/v) for quantification of the analyte, where a calibration curve was constructed with seven levels of testosterone using testosterone- $\text{d}_3$  as an internal standard. LC-MS analysis was done in the positive ion mode on a 6500 plus QTRAP mass spectrometer (Sciex, Singapore) coupled to an LC-30AD UHPLC system (Shimadzu, Japan) with an Agilent Eclipse Plus C18 column (2.1  $\times$  100 mm, 1.8  $\mu\text{m}$ ) at its temperature of 40  $^\circ\text{C}$ , a

flow rate of 0.5 mL/min, and an injection volume of 10  $\mu\text{L}$ . Water (A) and acetonitrile (B), both containing 0.1% formic acid, were employed as mobile phases A and with a gradient of 50–90% B (0–7.5 min). Both testosterone and testosterone- $\text{d}_3$  were detected with  $m/z$  289.2  $\rightarrow$  97.3 and 292.0  $\rightarrow$  100.0, respectively.

Other hormone levels in mice were quantified using commercially available ELISA kits, following the manufacturers' instructions. The specific kits used were: AMH (Ansh Labs, AL-113, TX, USA), FSH (Elabscience, E-EL-M0511, Wuhan, China), LH (Elabscience, E-EL-M3053), and insulin (Crystal Chem, 90080, IL, USA).

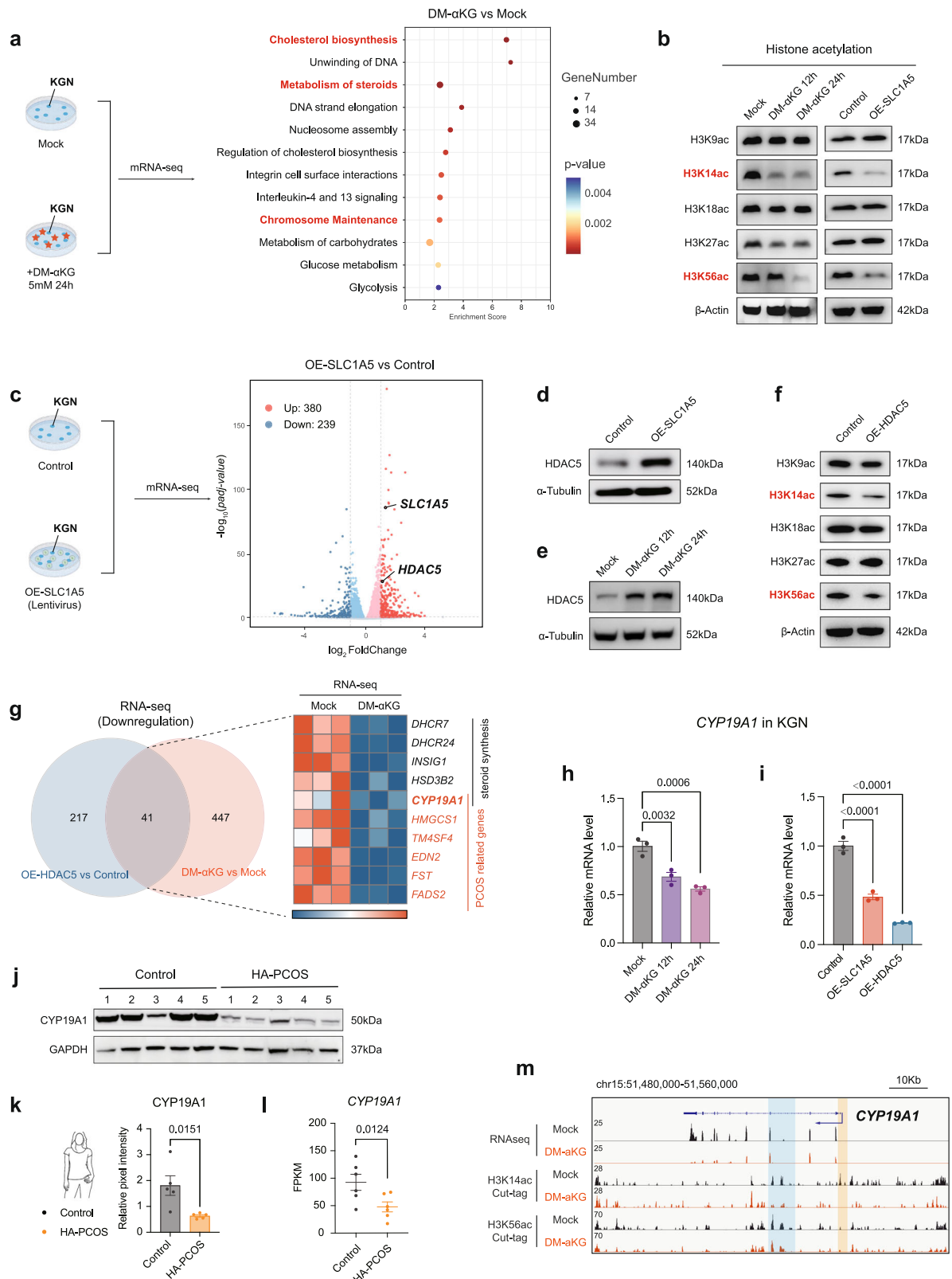
To evaluate reproductive competency, 8-week-old female mice were continuously mated with 10- to 12-week-old fertile males over 15 weeks. The number of pups and litters was recorded, and the fertility index was calculated as Handelsman et al. reported<sup>47</sup>. To evaluate ovarian response to exogenous gonadotropins, 7-week-old female mice were intraperitoneally injected with 5 IU of PMSG (AibeBio, Nanjing, China). After 44–48 h, GV oocytes were collected from antral follicles by puncturing with a 26.5-gauge needle. The ratio of the first polar body (pb1) extrusion was detected after 12 h of culture. For collecting MII oocytes, 7-week-old female mice were intraperitoneally injected with 5 IU of PMSG (AibeBio) followed by 5 IU of hCG (AibeBio). At 13–14 h after hCG injection, MII oocytes were retrieved and counted, which were then transferred to human tubal fluid (Sigma-Aldrich) and incubated with freshly prepared sperm, collected from fertile 10- to 12-week-old males. The number of 2-cell stage embryos was recorded to determine fertilization efficiency at 28 h after fertilization.

### Assessment of metabolic phenotypes

Mice were fasted for 12 h before the GTT and 4 h before the ITT. The glucose concentration was checked by tail vein blood sampling using the Accu-Chek Performa blood glucose meter (Roche, CA, USA). After testing the fasting glucose concentrations, the mice were intraperitoneally injected with glucose (2 mg/g body weight, Sigma-Aldrich) for the GTT, or insulin (0.75 IU/g body weight, Novo Nordisk, Copenhagen, Denmark) for the ITT. The tail sample blood glucose levels were measured at time points 0, 15, 30, 60, 90, and 120 mins for GTT, and 0, 15, 30, 45, 60, and 90 mins for ITT. Body weight was recorded per day. The measurement of adipose tissue mass, lean body mass, and total body water content was obtained using the small animal composition analyzer (Niumag, QMR06-090H, Suzhou, China), following the manufacturer's protocol. Blood was collected following 8 h of fasting, and serum was separated by centrifugation. Levels of total cholesterol, triglycerides, high-density lipoprotein cholesterol (HDL-C), and low-density lipoprotein cholesterol (LDL-C) were measured using commercially available assay kits (Nanjing Jiancheng Bioengineering Institute, China) according to the manufacturer's instructions.

### Cell culture

The human cell line HEK293T was purchased from ATCC, and KGN was a gift from the laboratory of Prof. Peter C.K. Leung (Children's Hospital Research Institute of British Columbia, Canada), and the cells were preserved in the central laboratory of the International Peace Maternity and Child Health Hospital. HEK293T cells were supposed to be cultured in Dulbecco's modified Eagle medium (DMEM, Gibco, NY,



USA) with 10% fetal bovine serum (FBS, Gibco) and 1% penicillin-streptomycin. KGN cells were cultured in DMEM/F12 (Gibco) with 10% FBS and 1% penicillin-streptomycin (Gibco).

**Glutamine uptake ratio assay**

KGN cells were cultured in serum-free DMEM/F12 medium and treated with 4 mM Gln for 24 h. Gln concentration in the medium was measured using a Gln assay kit (Abcam, ab197011, MA, USA). Cell counts

were determined using a Countess cell counter (Invitrogen, CA, USA). The Gln uptake ratio is calculated as (C1-C2)/Cell count, where C1 is the initial concentration of Gln, and C2 is the concentration of Gln in the medium after 24 h of incubation.

**Plasmids and lentivirus transfection**

The plasmids and lentiviral vectors were purchased commercially (Genechem, Shanghai, China). Transfection of plasmids into

**Fig. 7 | H3K14ac and H3K56ac mediate HDAC5 and  $\alpha$ -KG action regarding *CYP19A1* expression.** **a** Reactome pathway analysis of DEGs from RNA-seq analysis in DM- $\alpha$ KG-treated (5 mM, 24 h) KGN cells ( $n = 3$ ). **b** WB of histone acetylation in mock and DM- $\alpha$ KG-treated KGN cells, and Control and OE-SLC1A5, with  $\beta$ -Actin as reference. **c** Volcano plot of DEGs from RNA-seq analysis in Control and OE-SLC1A5 KGN cells ( $n = 3$ ), highlighting upregulated (red) and downregulated (blue) genes ( $|\log_2FC| > 1$ ,  $p_{adj} < 0.05$ ). **d** WB of HDAC5 expression in Control and OE-SLC1A5 KGN cells, with  $\alpha$ -Tubulin as reference. **e** WB of HDAC5 expression in Mock and DM- $\alpha$ KG-treated-KGN cells.  $\alpha$ -Tubulin was denoted as an internal reference protein. **f** WB analysis of histone acetylation levels in Control and OE-HDAC5 KGN cells, with  $\beta$ -Actin as reference. **g** Venn diagram and heatmap comparing DEGs from RNA-seq in OE-HDAC5/Control and DM- $\alpha$ KG/mock KGN cells ( $n = 3$ ). **h** *CYP19A1* expression in Mock and DM- $\alpha$ KG-treated KGN cells by qPCR

( $n = 3$ ). **i** *CYP19A1* expression in Control, OE-SLC1A5, and OE-HDAC5 in KGN cells by qPCR ( $n = 3$ ). **j**, **k** WB (**j**) and densitometric analysis (**k**) of *CYP19A1* in human GCs from Control and HA-PCOS ( $n = 5$ ), with GAPDH as reference. **l** FPKM of *CYP19A1* in human GCs from Control and HA-PCOS by RNA-seq ( $n = 5$ ). **m** CUT & Tag analysis of H3K14ac and H3K56ac binding peaks in DM- $\alpha$ KG-treated KGN cells, with *CYP19A1* promoter (yellow) and enhancer (blue) regions highlighted. The experiment was repeated three times independently in (**b**, **d-f**, and **j**) with similar results. For statistical analysis, DESeq2 was used in (**a**, **c**, **l**), with the Benjamini-Hochberg method applied for multiple testing correction in (**a**, **c**); one-way ANOVA followed by Dunnett's tests was performed in (**h**, **i**); and Student's *t* tests were performed in (**k**). Data are presented as the mean  $\pm$  SEM. All tests were two-sided. Source data are provided as a Source Data file.

HEK293T cells was carried out in 6-well plates. Cells were seeded in 6-well plates 24 h before transfection, reaching approximately 80% confluency by the time of the procedure. Following the manufacturer's instructions, 4  $\mu$ g of plasmid and 5  $\mu$ L Lipo2000 (Invitrogen) were used for transfection. Cells were collected 36 h after transfection. Before lentivirus transfection, KGN cells were seeded into 6-well plates 24 h before transfection with the lentivirus, and the medium was replaced with fresh DMEM/F12 after 8 h of incubation. To assess mRNA and protein expression, qPCR and western blot analyses were performed.

### Western blot analysis

Cells were lysed in SDT buffer (4% (w/v) SDS, 100 mM Tris/HCl, 1 mM DTT, pH 7.6) and denatured at room temperature for 30 min. Protein lysates (30  $\mu$ g total protein per lane) were separated by SDS-PAGE and transferred electrophoretically to PVDF membranes (Millipore, MA, USA). The membranes were blocked in TBST containing 5% skim milk (BD, NJ, USA) for 30 min. Following incubation with primary antibodies, the membranes were washed with TBST 3 times and then incubated with the HRP-linked secondary antibody (Jackson ImmunoResearch Laboratories, PA, USA) for 1 h, followed by three washes with TBST. Bound antibodies were detected using the Super Signal West Femto maximum sensitivity substrate (Thermo Scientific).

### RNA isolation and real-time qPCR analysis

Total RNA was isolated using the FastPure Cell/Tissue Total RNA Isolation Kit V2 (Vazyme, RC112, Nanjing, China) according to the manufacturer's instructions. Reverse transcription of 1  $\mu$ g of RNA was performed with the HiScript III All-in-one RT SuperMix Perfect for qPCR (Vazyme, R333). The quantitative PCR was performed using cDNA templates diluted in nuclease-free water, with amplification and detection carried out on the QuantStudio 7 Flex Real-Time PCR System (Life Technologies, CA, USA). All samples were analyzed in triplicate. Gene expression levels were normalized to those of the housekeeping genes *GAPDH* or *ACTB*. The primers used are listed in Supplementary Data 2.

### mRNA sequencing analysis

Cells were treated with TRIzol LS (Thermo Scientific) for RNA extraction. RNA integrity was assessed using the RNA Nano 6000 Assay Kit and Bioanalyzer 2100 system (Agilent) to ensure high-quality RNA. mRNA was purified from total RNA using poly-T magnetic beads. After fragmentation, first-strand cDNA was synthesized using random hexamer primers, followed by second-strand synthesis. The cDNA library underwent end repair, A-tailing, adapter ligation, size selection, amplification, and purification. Library quality was checked using Qubit, real-time PCR, and a Bioanalyzer. Libraries were clustered using the cBot system and sequenced on an Illumina Novaseq platform at Novogene Co., LTD (Beijing, China) and Genewiz (Suzhou, China), and 150 bp paired-end reads were generated. Differential expression analysis was performed using DESeq2 (v1.20.0), with false discovery rate (FDR) adjustment of *p*-values based on the Benjamini-Hochberg method ( $p_{adj} < 0.05$ ). Significantly differentially expressed genes

were defined as those exhibiting a fold change (FC)  $> 1.5$  in clinical GCs and FC  $> 2$  in KGN cells (Supplementary Data 3).

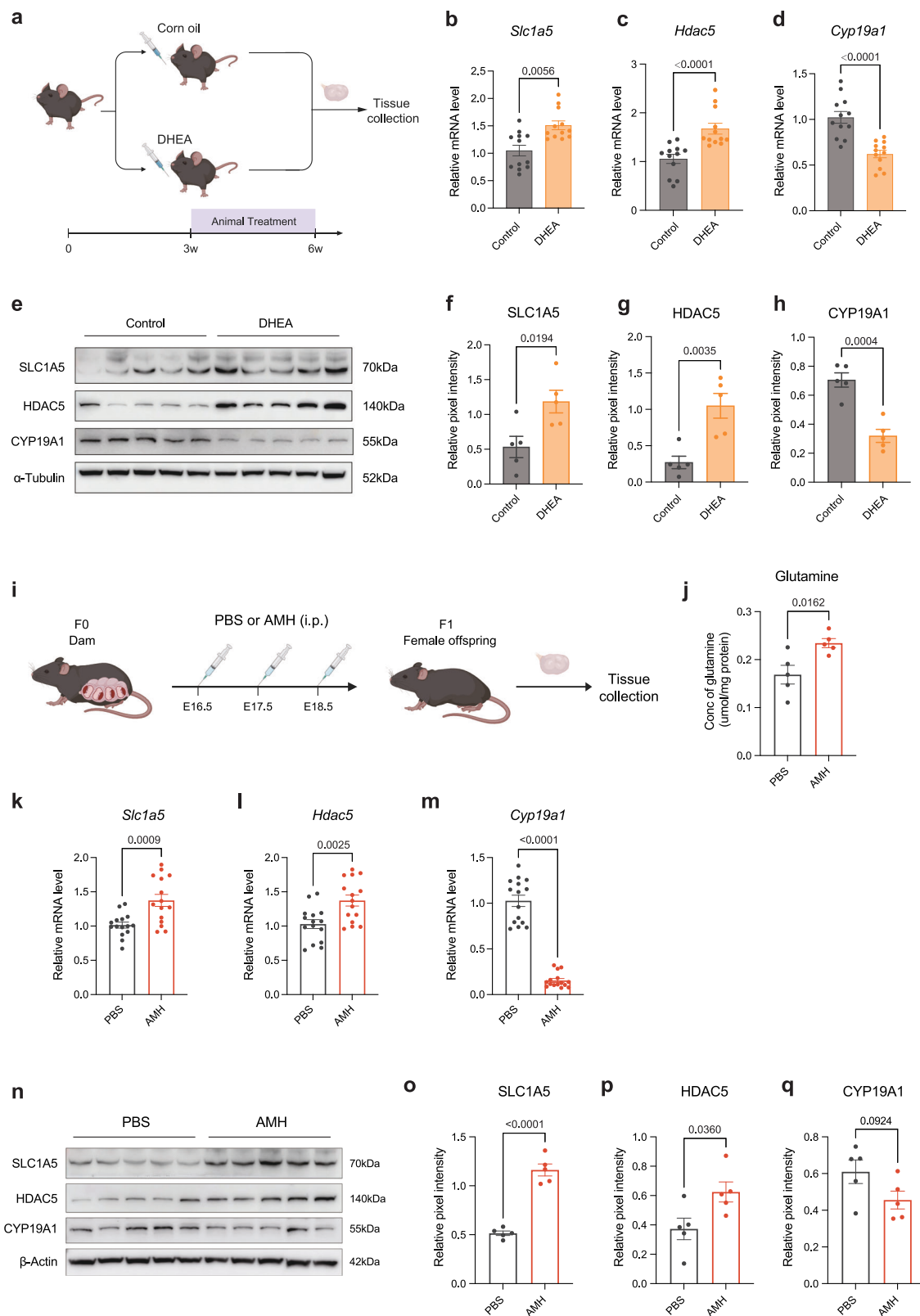
### CUT & Tag

CUT & Tag was performed using the Hyperactive Universal CUT & Tag Assay Kit for Illumina Pro (Vazyme, TD904), according to the manufacturer's instructions. About  $1.0 \times 10^5$  cells were collected, attached to concanavalin A-coated beads, and resuspended in antibody buffer solution. Cells were subsequently treated with primary antibodies, followed by incubation with secondary antibodies. Transposon activation and tagmentation were then performed, after which DNA was extracted, amplified, and purified to create the library. The library was quantified using qubit and sequenced on an Illumina NovaSeq platform at Novogene Co., LTD, and 150 bp paired-end reads were generated.

Raw data in fastq format were first processed using fastp (v 0.20.0). In this step, clean data were obtained by removing reads containing adapters, reads containing poly-N, and low-quality reads from raw data. At the same time, Q20, Q30, and GC content of the clean data were calculated. All the downstream analyses were based on the clean data. Reference genome and gene annotation files were downloaded from the genome website directly. Index of the reference genome was built using bwa (v 0.7.12), and clean reads were aligned to the reference genome using bwa mem -k 32 -T 30 -t 4 -M. The human reference genome was hg19. These reads were then filtered for high quality (MAPQ  $\geq 13$ ), and we also removed reads that were not properly paired and with PCR duplicates. Only uniquely mapped (MAPQ  $\geq 13$ ) and de-duplicated reads were used for further analysis. All peak calling was performed with MACS2<sup>56</sup> (v 2.1.0) using 'macs2 -q 0.05 -f AUTO-calls - nomodel - shift - 100 - extsize 200 - keep - dup all'. By default, peaks with a q-value threshold of 0.05 were used for all data sets. The genomic positions of peak summits relative to transcription start sites (TSS) were analyzed to predict protein-DNA interaction sites. Peak-associated genes were identified and annotated using ChIPseeker<sup>57</sup>, which determines the nearest genes to each peak and characterizes their genomic features.

### Stacc-seq

Approximately 1000 fresh 293 T cells were harvested. After adding 6  $\mu$ L DB-1 buffer (10 mM Tris-HCl, pH 7.4; 150 mM NaCl; 0.5 mM spermidine; 1 $\times$  EDTA-free protease inhibitor; 5% digitonin), cells were vortexed and incubated at 4  $^{\circ}$ C for 10 min. Antibody-pA/G-Tn5 complexes were prepared with 7  $\mu$ L DB-1 buffer, 0.5  $\mu$ L pA/G-Tn5, and 0.5  $\mu$ g antibody, incubated at 4  $^{\circ}$ C for 30 min. This mixture was added to the cells, and 12.5  $\mu$ L pre-warmed 5 $\times$  TTBL, incubated at 37  $^{\circ}$ C for 30 min. DNA was purified with phenol-chloroform, precipitated with ethanol and glycogen, and resuspended in ddH<sub>2</sub>O. PCR was performed to amplify the libraries (Vazyme, TD601) using the following PCR conditions: 72  $^{\circ}$ C for 3 min; 98  $^{\circ}$ C for 30 s; thermocycling for 16 cycles at 98  $^{\circ}$ C for 15 s, 60  $^{\circ}$ C for 30 s and 72  $^{\circ}$ C for 3 min; followed by 72  $^{\circ}$ C for 5 min. After the PCR reaction, libraries were purified by 0.4 $\times$ -1.7 $\times$  AMPure beads size selection and were subjected to next-generation sequencing.



### Measurement of cell proliferation

Cells were seeded into 96-well culture plates at a density of 2000 cells per well. After cell attachment, the medium was replaced, and corresponding treatments were applied. Relative cell growth was measured using a Cell Counting Kit-8 (Beyotime, Shanghai, China) according to the manufacturer's protocol.

### Measurement of GSH/GSSG ratio, ROS, mitochondrial ROS, and mitochondrial membrane potential

The ratio of reduced GSH to oxidized glutathione (GSSG) was measured by the GSH/GSSH assay kit (Abcam, ab205811) with the fluorescence (Ex/Em: 490/520 nm) recorded, following the manufacturer's instructions. Changes in intracellular ROS were detected by

**Fig. 8 | The levels of SLC1A5, HDAC5, and CYP19A1 in the ovaries of DHEA-induced PCOS-like and PAMH mice.** **a** Schematic diagram of the DHEA-induced PCOS-like model. Created in BioRender. Ye, L. (2025) <https://BioRender.com/yb2yu8f>. **b–d** mRNA expression of *Slc1a5* (**b**), *Hdac5* (**c**), and *Cyp19a1* (**d**) in ovaries collected from Control and DHEA-treated mice determined by qPCR ( $n = 12$  for each group). **e–h** Western blots (**e**) and densitometric analysis of SLC1A5 (**f**), HDAC5 (**g**), and CYP19A1 (**h**) expression relative to  $\alpha$ -Tubulin in the ovaries of Control and DHEA-treated mice ( $n = 5$  for each group). **i** Schematic diagram of the PAMH model. Created in BioRender. Ye, L. (2025) <https://BioRender.com/Owojt74>. **j** Levels of

glutamine in the ovaries of F1 female offspring of PBS and AMH-treated ( $n = 5$  for each group) dams. **k–m** mRNA expression of *Slc1a5* (**k**), *Hdac5* (**l**) and *Cyp19a1* (**m**) in the ovaries of F1 female offspring of PBS and AMH-treated dams determined by qPCR ( $n = 15$  for each group). **n–q** Western blots (**n**) and densitometric analysis of SLC1A5 (**o**), HDAC5 (**p**) and CYP19A1 (**q**) expression relative to  $\beta$ -Actin in the ovaries of PBS and AMH-treated mice ( $n = 5$  for each group). For statistical analysis, Mann-Whitney tests were performed in (**b**, **c**, **m**); and Student's *t* tests were performed in (**d**, **f–h**, **j–l**, **o–q**). All tests were two-sided. The biological replicates are used for statistical analysis in (**b–h**, **j–q**). Source data are provided as a Source Data file.

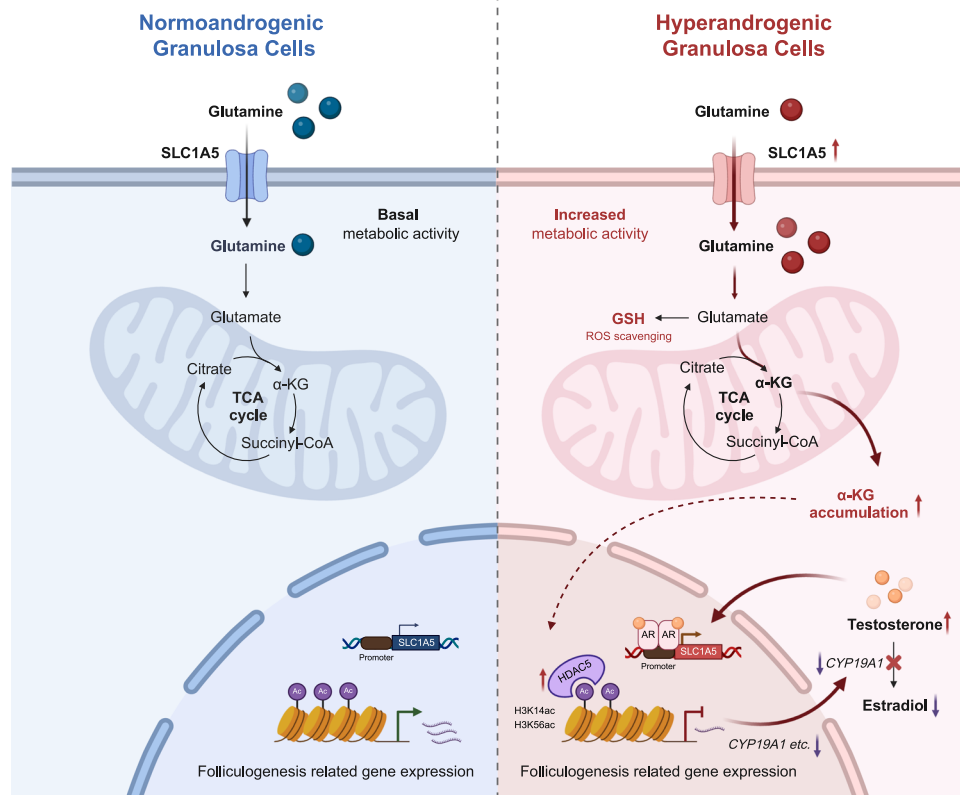


**Fig. 9 | The graph model of the role of SLC1A5 in granulosa cells under physiological versus hyperandrogenic PCOS conditions.** In hyperandrogenic granulosa cells, elevated androgen levels directly enhance AR binding to the *SLC1A5* promoter, driving its transcriptional activation and upregulating *SLC1A5* expression. This hyperactivation enhances glutamine uptake, leading to excessive  $\alpha$ -KG accumulation. The surplus  $\alpha$ -KG interacts with histone deacetylase 5 (HDAC5), resulting in global hypoacetylation (reduced H3K14ac and H3K56ac). This

epigenetic repression downregulates *CYP19A1* and other folliculogenesis-related genes. Critically, *CYP19A1* suppression disrupts the aromatase-mediated conversion of androgens to estrogens. Thus, a pathological feedforward loop is established: hyperandrogenism reinforces AR-driven *SLC1A5* overexpression, which in turn exacerbates hyperandrogenism. This self-sustaining cycle perpetuates ovarian dysfunction in PCOS. Created in BioRender. Ye, L. (2025) <https://BioRender.com/t27l890>.

incubation of living cells with  $1 \mu\text{M}$  of H2DCFDA (Ex/Em: 492/517 nm, Invitrogen, D399) for 15 min. Mitochondrial ROS were detected by staining cells with  $5 \mu\text{M}$  MitoSOX Red mitochondrial superoxide indicator (Ex/Em: 510/580 nm, Invitrogen, M36008) as per the manufacturer's protocol. Mitochondrial membrane potential (MMP) was evaluated by incubating cells with  $20 \text{ nM}$  TMRE (Invitrogen, T669) for 15 minutes. Stained cells were analyzed using a flow cytometer (BD FACSCelesta).

#### Measurement of ECAR and OCR

The measurement of ECAR and OCR was carried out using an XF96 extracellular flux analyzer (Agilent). Before assay, 8000 KGN cells were seeded per well in 96-well micro cell culture plates (Agilent) in DMEM/F12 with 10% FBS. After basal measurements, cells were treated with oligomycin ( $1.5 \mu\text{M}$ ) and FCCP ( $2 \mu\text{M}$ ) to assess maximal OCR. What's more, cells were treated with Rotenone/Antimycin ( $0.5 \mu\text{M}$ ) to access maximal ECAR. Every measurement involved 3 min of mixing, 3 min of

incubation, and 4 min of recording data. The resulting ECAR and OCR values were adjusted based on cell count and analyzed using WAVE software (Agilent).

#### Analysis of the metabolic flux

For the metabolic flux analysis, L-glutamine ( $^{13}\text{C}_5$ , 99%) was procured from Cambridge Isotope Laboratories (MA, USA). Cells were cultured in DMEM/F12 medium containing  $4 \text{ mM}$  L-glutamine ( $^{13}\text{C}_5$ , 99%), 10% FBS, and 1% penicillin-streptomycin for 24 h before cell pellet collection. Following collection, the samples were vortexed for 20 s, incubated in liquid nitrogen for 1 min, and then sonicated for 6 min. After a 1.5 h incubation at  $37^\circ\text{C}$ , the samples were centrifuged, and the supernatant was harvested for subsequent GC-MS analysis.

The GC analysis was conducted on an HP-5MS column ( $30 \text{ m} \times 0.25 \mu\text{m} \times 0.25 \mu\text{m}$ , Agilent) utilizing a GC/MSD instrument (Agilent, 7890-5977B) as described previously<sup>58</sup>. The injector temperature was maintained at  $260^\circ\text{C}$ . The column oven temperature was initially set at

70 °C for 2 min, followed by a gradual increase to 180 °C at a rate of 7 °C/min, then to 250 °C at 5 °C/min, and finally to 310 °C at 25 °C/min, where it was held for 15 min. The MSD transfer line temperature was set at 280 °C, while the MS quadrupole and ion source temperatures were maintained at 150 °C and 230 °C, respectively. Measurements were performed in both scan mode (to ensure the quality and purity of each TCA intermediate peak) and selected ion monitoring (SIM) mode (to maximize the sensitivity of GC-MS for quantifying each metabolite/isotopomer). In SIM mode, the fragment ion with an  $m/z$  of  $[M-57]$  (where M represents the molecular mass of each derivatized metabolite, and  $-57$  corresponds to the loss of the tert-butyl moiety during GC analysis) was designated as the quantitative ion for each compound. To capture all potential isotopomer peaks, including those of naturally occurring isotopes of specific metabolites (with  $n$  carbon atoms), the  $m/z$  range from  $[M-57]$  to  $[M-57] + n + 1$  was included during data acquisition. In particular, for  $\alpha$ -KG, the  $m/z$  range was extended to  $[M-57] + n + 2$  due to the oximation process during derivatization. The following  $m/z$  values were employed for each compound: succinate (289, 290, 291, 292, 293); fumarate (287, 288, 289, 291, 292);  $\alpha$ -KG (346, 347, 348, 349, 350, 351, 352); malate (419, 420, 421, 422, 423); Glu (432, 433, 434, 435, 436, 437); Gln (431, 432, 433, 434, 435, 436); citrate (591, 592, 593, 594, 595, 596, 597); and myristic acid (312) as the internal standard.

Data acquisition was performed using MassHunter GC/MS Acquisition software (Agilent). For quantification, peaks were extracted and integrated using GC-MS MassHunter Workstation Qualitative Analysis software (Agilent), with natural isotope corrections applied using IsoCor<sup>59</sup> software in matrix-based mode. The protein wet weight of each sample was determined via the Bradford assay after dissolving the naturally dried protein sediment in 0.2 M KOH at room temperature.

### Immunofluorescence staining

Cultured cells were rinsed with PBS and then fixed in 4% paraformaldehyde (PFA) for 15 min. After washing with PBS, the cells were permeabilized with 1% Triton-100 for 15 min and then blocked with 3% bovine serum albumin for 1 h. After blocking, the cells were incubated overnight at 4 °C with the primary antibody. After washing with PBS, the cells were treated with Alexa Fluor 488-conjugated secondary antibodies (Invitrogen) for 1 h and subsequently stained with 4',6-diamidino-2-phenylindole (DAPI, Invitrogen) at room temperature. IF was examined using an SP8 Confocal Microscope and LAS X Image processing software (Leica).

### Immunohistochemistry staining

Tissue sections were deparaffinized in xylene and rehydrated. Antigen retrieval was performed in citrate buffer (pH 6.0) using a microwave. After cooling, sections were blocked with 5% BSA in PBS for 1 h. Primary antibodies were applied overnight at 4 °C, followed by HRP-conjugated secondary antibodies for 1 h at room temperature. Visualization was achieved using a DAB substrate kit, and sections were counterstained with hematoxylin and mounted for microscopy. Negative controls omitted the primary antibody.

### Transmission electron microscopy analysis

Cells were collected after centrifugation and fixed in 2.5% glutaraldehyde solution at 4 °C. The fixed samples were centrifuged, washed three times in 0.1 M phosphate buffer (PB, pH 7.4), and then embedded in 1% agarose. Post-fixation was performed with 1% osmium tetroxide ( $\text{OsO}_4$ ) in 0.1 M PB for 2 h at room temperature, followed by three 15-min rinses in PB. The samples were dehydrated through a graded ethanol series (30%, 50%, 70%, 80%, 95%, and 100%) and acetone, then infiltrated with increasing concentrations of EMBED 812 resin. After embedding in pure resin, samples were polymerized at 60 °C for 48 h. Ultrathin sections (60–80 nm) were cut with an ultramicrotome Leica

UC7 and collected on 150-mesh copper grids with formvar film. Sections were stained with 2% uranyl acetate and lead citrate, then washed and dried. TEM images were captured after observation under a transmission electron microscope HITACHI HT7800 (Hitachi High-Tech Corporation, Hitachinaka, Japan).

### Quantifying follicular numbers within the mouse ovary

Ovaries were fixed overnight in 10% PBS buffered formalin and then embedded in paraffin. Thin paraffin sections (4  $\mu\text{m}$ ) were serially cut, collected at regular intervals (every 4th section), and stained with HE for direct follicle counts. The number of follicles was determined by recording the number of oocyte nuclei in all sections<sup>60,61</sup>. Follicles were classified as primordial if they contained an oocyte surrounded by a partial or complete layer of squamous GCs. Primary follicles showed a single layer of cuboidal GCs. Occasional follicles were observed as intermediate between primordial and primary and had both cuboidal and squamous GCs. If cuboidal cells predominated follicles were classified as the primary type. Follicles were classed as secondary if they possessed more than one layer of GCs with no visible antrum. Early antral follicles generally possessed only one or two small areas of FF (antrum), whilst antral follicles possessed a single large antral space. Pre-ovulatory follicles had a rim of cumulus cells surrounding the oocyte. Corpus luteum typically displays large nuclei and lipid droplets in the cytoplasm.

### Quantification and statistical analysis

Data are presented as mean  $\pm$  standard error of the mean (SEM). Normality and homogeneity of variances were assessed using the Shapiro-Wilk and Brown-Forsythe tests, respectively. For comparisons between two groups, normally distributed data with equal variances were analyzed using a two-tailed unpaired Student's *t*-test, while non-normally distributed data or data with unequal variances were assessed using the Mann-Whitney U test. For comparisons among multiple groups, one-way ANOVA with Tukey's post hoc test was used for normally distributed data with equal variances; the Kruskal-Wallis test with Dunn's multiple comparisons test was used for non-normally distributed data. When data were normally distributed but exhibited unequal variances, Welch's ANOVA followed by Dunnett's T3 multiple comparisons test was applied. For experiments involving two independent variables, two-way ANOVA was used, followed by Tukey's multiple comparisons test. All statistical analyses were performed using GraphPad Prism version 10. A *P* value  $< 0.05$  was considered statistically significant.

### Reporting summary

Further information on research design is available in the Nature Portfolio Reporting Summary linked to this article.

### Data availability

All the data relating to RNA sequencing and CUT & Tag of this study have been uploaded to the Sequence Read Archive database and are available for download via accession numbers [PRJNA1172636](#), [PRJNA1172872](#), [PRJNA1173315](#), [PRJNA1173322](#), [PRJNA1173369](#), and [PRJNA1244852](#). The raw metabolomic data have been deposited in the MetaboLights database under accession numbers [MTBLS12367](#), [MTBLS12370](#), and [MTBLS12371](#) for public access. The raw data of metabolic flux analysis are shown in Supplementary Data 4. Source data are provided with this paper. Further information and requests for resources and reagents should be directed to and will be fulfilled by the lead contact, Hefeng Huang ([huanghefg@hotmail.com](mailto:huanghefg@hotmail.com)). Source data are provided with this paper.

### References

1. Boyle, J. A. & Teede, H. J. Refining diagnostic features in PCOS to optimize health outcomes. *Nat. Rev. Endocrinol.* **12**, 630–631 (2016).

2. Unluhizarci, K., Karaca, Z. & Kelestimur, F. Role of insulin and insulin resistance in androgen excess disorders. *World J. Diabetes* **12**, 616–629 (2021).
3. Joham, A. E. et al. Polycystic ovary syndrome. *Lancet Diabetes Endocrinol.* **10**, 668–680 (2022).
4. Teede, H. J. et al. Recommendations from the 2023 international evidence-based guideline for the assessment and management of polycystic ovary syndrome. *J. Clin. Endocrinol. Metab.* **108**, 2447–2469 (2023).
5. Escobar-Morreale, H. F. Polycystic ovary syndrome: Definition, aetiology, diagnosis and treatment. *Nat. Rev. Endocrinol.* **14**, 270–284 (2018).
6. Wang, Y., Leung, P., Li, R., Wu, Y. & Huang, H. Editorial: Polycystic ovary syndrome (PCOS): mechanism and management. *Front. Endocrinol.* **13**, 1030353 (2022).
7. Wang, Y., Leung, P., Li, R., Wu, Y. & Huang, H. Editorial: Polycystic ovary syndrome: mechanism and management-volume II. *Front. Endocrinol.* **14**, 1247679 (2023).
8. Dumesic, D. A. et al. Scientific statement on the diagnostic criteria, epidemiology, pathophysiology, and molecular genetics of polycystic ovary syndrome. *Endocr. Rev.* **36**, 487–525 (2015).
9. Canipari, R. Oocyte–granulosa cell interactions. *Hum. Reprod. Update* **6**, 279–289 (2000).
10. Richani, D., Dunning, K. R., Thompson, J. G. & Gilchrist, R. B. Metabolic co-dependence of the oocyte and cumulus cells: Essential role in determining oocyte developmental competence. *Hum. Reprod. Update* **27**, 27–47 (2021).
11. Chang, H.-M., Qiao, J. & Leung, P. C. K. Oocyte-somatic cell interactions in the human ovary—novel role of bone morphogenetic proteins and growth differentiation factors. *Hum. Reprod. Update* **23**, 1–18 (2016).
12. Liu, X. et al. Novel PGK1 determines SKP2-dependent AR stability and reprograms granular cell glucose metabolism facilitating ovulation dysfunction. *EBioMedicine* **61**, 103058 (2020).
13. Liao, B., Qi, X., Yun, C., Qiao, J. & Pang, Y. Effects of androgen excess-related metabolic disturbances on granulosa cell function and follicular development. *Front. Endocrinol.* **13**, 815968 (2022).
14. Ye, Z. et al. Amino acid signatures in relation to polycystic ovary syndrome and increased risk of different metabolic disturbances. *Reprod. Biomed. Online* **44**, 737–746 (2022).
15. Mu, L. et al. PPM1K-regulated impaired catabolism of branched-chain amino acids orchestrates polycystic ovary syndrome. *EBioMedicine* **89**, 104492 (2023).
16. Zhang, K.-H. et al. Follicle stimulating hormone controls granulosa cell glutamine synthesis to regulate ovulation. *Protein Cell* **15**, pwad065 (2024).
17. Scalise, M., Pochini, L., Galluccio, M., Console, L. & Indiveri, C. Glutamine transporters as pharmacological targets: From function to drug design. *Asian J. Pharm. Sci.* **15**, 207–219 (2020).
18. Cardoso, H. J. et al. Glutaminolysis is a metabolic route essential for survival and growth of prostate cancer cells and a target of 5 $\alpha$ -dihydrotestosterone regulation. *Cell. Oncol. Dordr. Neth.* **44**, 385–403 (2021).
19. White, M. A. et al. Glutamine transporters are targets of multiple oncogenic signaling pathways in prostate cancer. *Mol. Cancer Res. MCR* **15**, 1017–1028 (2017).
20. Kempegowda, P., Melson, E., Manolopoulos, K. N., Arlt, W. & O'Reilly, M. W. Implicating androgen excess in propagating metabolic disease in polycystic ovary syndrome. *Ther. Adv. Endocrinol. Metab.* **11**, 2042018820934319 (2020).
21. Azziz, R. et al. Polycystic ovary syndrome. *Nat. Rev. Dis. Prim.* **2**, 16057 (2016).
22. Mohammad, M. B. & Seghinsara, A. M. Polycystic ovary syndrome (PCOS), diagnostic criteria, and AMH. *Asian Pac. J. Cancer Prev. APJCP* **18**, 17–21 (2017).
23. Yang, Z. et al. Steroid metabolome profiling of follicular fluid in normo- and hyperandrogenic women with polycystic ovary syndrome. *J. Steroid Biochem. Mol. Biol.* **206**, 105806 (2021).
24. Yang, L., Venneti, S. & Nagrath, D. Glutaminolysis: A hallmark of cancer metabolism. *Annu. Rev. Biomed. Eng.* **19**, 163–194 (2017).
25. Son, J. et al. Glutamine supports pancreatic cancer growth through a KRAS-regulated metabolic pathway. *Nature* **496**, 101–105 (2013).
26. Cm, M. et al. Reductive glutamine metabolism by IDH1 mediates lipogenesis under hypoxia. *Nature* **481**, 380–384 (2011).
27. Son, J. et al. Glutamine-driven oxidative phosphorylation is a major ATP source in transformed mammalian cells in both normoxia and hypoxia. *Mol. Syst. Biol.* **9**, 712 (2013).
28. Anderson, N. M., Mucka, P., Kern, J. G. & Feng, H. The emerging role and targetability of the TCA cycle in cancer metabolism. *Protein Cell* **9**, 216–237 (2018).
29. Kang, H. S. et al. IDH1-dependent  $\alpha$ -KG regulates brown fat differentiation and function by modulating histone methylation. *Metabolism* **105**, 154173 (2020).
30. Carey, B. W., Finley, L. W. S., Cross, J. R., Allis, C. D. & Thompson, C. B. Intracellular  $\alpha$ -ketoglutarate maintains the pluripotency of embryonic stem cells. *Nature* **518**, 413–416 (2015).
31. Andonegui-Elguera, M. A. et al. The roles of histone post-translational modifications in the formation and function of a mitotic chromosome. *Int. J. Mol. Sci.* **23**, 8704 (2022).
32. Karmodiya, K., Krebs, A. R., Oulad-Abdelghani, M., Kimura, H. & Tora, L. H3K9 and H3K14 acetylation co-occur at many gene regulatory elements, while H3K14ac marks a subset of inactive inducible promoters in mouse embryonic stem cells. *BMC Genomics* **13**, 424 (2012).
33. Cote, J. M. et al. Two factor authentication: Asf1 mediates crosstalk between h3 k14 and k56 acetylation. *Nucleic Acids Res* **47**, 7380–7391 (2019).
34. Topal, S., Vasseur, P., Radman-Livaja, M. & Peterson, C. L. Distinct transcriptional roles for histone H3-K56 acetylation during the cell cycle in yeast. *Nat. Commun.* **10**, 4372 (2019).
35. Duan, M.-R. & Smerdon, M. J. Histone H3 lysine 14 (H3K14) acetylation facilitates DNA repair in a positioned nucleosome by stabilizing the binding of the chromatin remodeler RSC (remodels structure of chromatin). *J. Biol. Chem.* **289**, 8353–8363 (2014).
36. Blank, S. K., McCartney, C. R. & Marshall, J. C. The origins and sequelae of abnormal neuroendocrine function in polycystic ovary syndrome. *Hum. Reprod. Update* **12**, 351–361 (2006).
37. Guo, Y. et al. Polymorphisms of estrogen-biosynthesis genes CYP17 and CYP19 may influence age at menarche: A genetic association study in caucasian females. *Hum. Mol. Genet.* **15**, 2401–2408 (2006).
38. Franks, S., Stark, J. & Hardy, K. Follicle dynamics and anovulation in polycystic ovary syndrome. *Hum. Reprod. Update* **14**, 367–378 (2008).
39. Webber, L. J. et al. Formation and early development of follicles in the polycystic ovary. *Lancet Lond. Engl.* **362**, 1017–1021 (2003).
40. Zhang, C. L. et al. Class II histone deacetylases act as signal-responsive repressors of cardiac hypertrophy. *Cell* **110**, 479–488 (2002).
41. Zuelke, K. A. & Brackett, B. G. Increased glutamine metabolism in bovine cumulus cell-enclosed and denuded oocytes after in vitro maturation with luteinizing hormone. *Biol. Reprod.* **48**, 815–820 (1993).
42. Wasa, M., Wang, H. S., Tazuke, Y. & Okada, A. Insulin-like growth factor-I stimulates amino acid transport in a glutamine-deprived human neuroblastoma cell line. *Biochim. Biophys. Acta* **1525**, 118–124 (2001).
43. Das, M. et al. Granulosa cell survival and proliferation are altered in polycystic ovary syndrome. *J. Clin. Endocrinol. Metab.* **93**, 881–887 (2008).

44. Ashraf, S. et al. Impact of rs2414096 polymorphism of CYP19 gene on susceptibility of polycystic ovary syndrome and hyperandrogenism in Kashmiri women. *Sci. Rep.* **11**, 12942 (2021).
45. Windmueller, H. G. & Spaeth, A. E. Uptake and metabolism of plasma glutamine by the small intestine. *J. Biol. Chem.* **249**, 5070–5079 (1974).
46. Etchegaray, J.-P. & Mostoslavsky, R. Interplay between metabolism and epigenetics: A nuclear adaptation to environmental changes. *Mol. Cell* **62**, 695–711 (2016).
47. Erickson, G. F., Hsueh, A. J., Quigley, M. E., Rebar, R. W. & Yen, S. S. Functional studies of aromatase activity in human granulosa cells from normal and polycystic ovaries. *J. Clin. Endocrinol. Metab.* **49**, 514–519 (1979).
48. Jakimiuk, A. J., Weitsman, S. R., Brzechffa, P. R. & Magoffin, D. A. Aromatase mRNA expression in individual follicles from polycystic ovaries. *Mol. Hum. Reprod.* **4**, 1–8 (1998).
49. Mimouni, N. E. H. et al. Polycystic ovary syndrome is transmitted via a transgenerational epigenetic process. *Cell Metab.* **33**, 513–530.e8 (2021).
50. Kaelin, W. G. & McKnight, S. L. Influence of metabolism on epigenetics and disease. *Cell* **153**, 56–69 (2013).
51. Verdin, E. & Ott, M. 50 years of protein acetylation: From gene regulation to epigenetics, metabolism and beyond. *Nat. Rev. Mol. Cell Biol.* **16**, 258–264 (2015).
52. Bannister, A. J. & Kouzarides, T. Regulation of chromatin by histone modifications. *Cell Res* **21**, 381–395 (2011).
53. Tata, B. et al. Elevated prenatal anti-müllerian hormone reprograms the fetus and induces polycystic ovary syndrome in adulthood. *Nat. Med.* **24**, 834–846 (2018).
54. Xiao, J. et al. 25-Hydroxycholesterol regulates lysosome AMP kinase activation and metabolic reprogramming to educate immunosuppressive macrophages. *Immunity* **57**, 1087–1104.e7 (2024).
55. Hou, Z. et al. Inhibiting 3βHSD1 to eliminate the oncogenic effects of progesterone in prostate cancer. *Cell Rep. Med.* **3**, 100561 (2022).
56. Zhang, Y. et al. Model-based analysis of ChIP-Seq (MACS). *Genome Biol.* **9**, R137 (2008).
57. Yu, G., Wang, L.-G. & He, Q.-Y. ChIPseeker: an R/Bioconductor package for ChIP peak annotation, comparison and visualization. *Bioinforma. Oxf. Engl.* **31**, 2382–2383 (2015).
58. Qu, Q. et al. Lithocholic acid phenocopies anti-ageing effects of calorie restriction. *Nature* <https://doi.org/10.1038/s41586-024-08329-5> (2024).
59. Millard, P. et al. IsoCor: Isotope correction for high-resolution MS labeling experiments. *Bioinforma. Oxf. Engl.* **35**, 4484–4487 (2019).
60. Winship, A. L., Sarma, U. C., Alesi, L. R. & Hutt, K. J. Accurate follicle enumeration in adult mouse ovaries. *J. Vis. Exp. JoVE* <https://doi.org/10.3791/61782> (2020).
61. Myers, M., Britt, K. L., Wreford, N. G. M., Ebling, F. J. P. & Kerr, J. B. Methods for quantifying follicular numbers within the mouse ovary. *Reprod. Camb. Engl.* **127**, 569–580 (2004).
- China) and OeBiotech (Shanghai, China) for the detection of amino acids and their metabolites. We would like to thank the BioRender team for providing the tools that assisted us in creating the illustrations and figures for this study. This work was supported by the National Natural Science Foundation of China (82088102 to H.H.). We acknowledge the Key Discipline Construction Project (2023-2025) of the Three-Year Initiative Plan for Strengthening Public Health System Construction in Shanghai (GWVI-11.1-35 to H.H.), Shanghai Clinical Research Center for Gynecological Diseases (22MC1940200 to H.H.), Shanghai Urogenital System Diseases Research Center (2022ZZ01012 to H.H.), Shanghai Frontiers Science Research Center of Reproduction and Development (to H.H.), the National Key Research and Development Program of China (2024YFA180300 to G.D.), and the Fund of Fudan University and Cao'ejiang Basic Research (24FCA14 to G.D.).

## Author contributions

H.H., C.Y., G.D., and Y.Z. designed the experiments. Y.Wang, J.W., G.Z., and C.Y. performed the experiments. Y.Wang, H.H., C.Y., G.D., Y.Z., Y.S., and X.W. analyzed the data. Y.Wang, P.L., J.P., X.C., C.Z., Y.Wu, L.J., B.W., and J.W. collected the clinical samples and analyzed the characteristics of the clinical patients. Y.M., Z.Z., and W.H. performed partial experiments of supplemental data. Y.Wang wrote the paper with the help of J.S., X.L., C.Y., Y.Z., and G.D.

## Competing interests

The authors declare no competing interests.

## Additional information

**Supplementary information** The online version contains supplementary material available at <https://doi.org/10.1038/s41467-025-62951-z>.

**Correspondence** and requests for materials should be addressed to Yu Zhang, Guolian Ding, Chuanjin Yu or Hefeng Huang.

**Peer review information** *Nature Communications* thanks Anna Benrick, Kangling Zhang, and the other, anonymous, reviewer for their contribution to the peer review of this work. A peer review file is available.

**Reprints and permissions information** is available at <http://www.nature.com/reprints>

**Publisher's note** Springer Nature remains neutral with regard to jurisdictional claims in published maps and institutional affiliations.

**Open Access** This article is licensed under a Creative Commons Attribution-NonCommercial-NoDerivatives 4.0 International License, which permits any non-commercial use, sharing, distribution and reproduction in any medium or format, as long as you give appropriate credit to the original author(s) and the source, provide a link to the Creative Commons licence, and indicate if you modified the licensed material. You do not have permission under this licence to share adapted material derived from this article or parts of it. The images or other third party material in this article are included in the article's Creative Commons licence, unless indicated otherwise in a credit line to the material. If material is not included in the article's Creative Commons licence and your intended use is not permitted by statutory regulation or exceeds the permitted use, you will need to obtain permission directly from the copyright holder. To view a copy of this licence, visit <http://creativecommons.org/licenses/by-nc-nd/4.0/>.

© The Author(s) 2025

## Acknowledgements

The authors would like to thank Xinyu Li (The Ohio State University, USA) for his expert advice on the statistical analysis. The authors also appreciate the support from Pinjia Chen and Mo Zhang (Fudan University, China) for their support in bioinformatics analysis. We acknowledge that the analysis of serum TT was done by Prof. Huiru Tang's group, Fudan University, as a contracted service. Our sincere thanks go to Mingxia Zhu (Xiamen University, China) for her assistance with the tracing of <sup>13</sup>C Gln metabolic flux analysis using GC-MS. We are grateful to the Laboratory Animal Center of Shanghai Jiao Tong University for the care of model mice. We also thank MetWare (Wuhan,

<sup>1</sup>International Peace Maternity and Child Health Hospital, Shanghai Key Laboratory of Embryo Original Diseases, School of Medicine, Shanghai Jiao Tong University, Shanghai, China. <sup>2</sup>Institute of Reproduction and Development, Shanghai Key Laboratory of Reproduction and Development, Obstetrics and Gynecology Hospital, Fudan University, Shanghai, China. <sup>3</sup>Institute of Medical Genetics and Development, Key Laboratory of Reproductive Genetics (Ministry of Education) and Women's Hospital, Zhejiang University School of Medicine, Hangzhou, Zhejiang, China. <sup>4</sup>Department of Reproductive Medicine, Xinhua Hospital, School of Medicine, Shanghai Jiao Tong University, Shanghai, China. <sup>5</sup>Shanghai Key Laboratory of Female Reproductive Endocrine Related Diseases, Shanghai, China. <sup>6</sup>These authors contributed equally: Yishu Wang, Jiaying Wu. ✉e-mail: [zhang\\_yu\\_sfy@fudan.edu.cn](mailto:zhang_yu_sfy@fudan.edu.cn); [dingguolian@fudan.edu.cn](mailto:dingguolian@fudan.edu.cn); [yuchuanjin1013@163.com](mailto:yuchuanjin1013@163.com); [huanghefg@hotmail.com](mailto:huanghefg@hotmail.com)